Received: 28 April 2024 | Revised: 25 November 2024 | Accepted: 8 December 2024

DOI: 10.1002/suco.202400556

ARTICLE

fib CEB-FIP WILEY

Structural behavior of deteriorated Gerber half-joints in highway overpasses by nonlinear finite element analysis combined with a simplified uniform-corrosion model

Dario De Domenico[1] | **Nino Spinella**[2] | **Davide Messina**[1] | **Matteo Mazzeo**[1] | **Antonino Recupero**[1]

[1]Department of Engineering, University of Messina, Messina, Italy

[2]Department of Civil Engineering and Architecture, University of Catania, Catania, Italy

Correspondence
Dario De Domenico, Department of Engineering, University of Messina, Contrada Di Dio, 98166 Sant'Agata, Messina, Italy.
Email: dario.dedomenico@unime.it

Abstract

Gerber half-joints, broadly used in the last century as elements of concrete bridges, are prone to corrosion-induced deterioration, which may lead to brittle shear collapse. It is of paramount importance to develop advanced numerical models for simulating the collapse behavior of Gerber half-joints, taking material deterioration into account. This paper investigates the ultimate capacity of deteriorated Gerber half-joints belonging to a set of 50-year-old road overpasses in Messina, Italy. The peculiarities of these prestressed concrete bridges are: (1) oversized hangers and diagonal reinforcement bars in the dapped end; (2) inadequate concrete compressed area in the section above the pier subject to negative bending moment. Calibrated upon an extensive *in situ* test campaign, a parametric 2D and 3D nonlinear finite element analysis (NLFEA) of a portion of the bridge deck is performed to quantify model uncertainties related to: (i) modeling approach, involving different dimensions of the finite element (FE) model (2D and 3D), software, solvers, and implemented nonlinear concrete material model; (ii) shrinkage and creep formulation in the NLFEAs; (iii) effect of the transverse diaphragm in the section above the pier. Carbonation depths identified from experimental tests in conjunction with gravimetric analysis on extracted steel samples are used for calibrating a simplified uniform-corrosion model, which is incorporated in the NLFEA to investigate the influence of corrosion on the load-bearing capacity and failure mechanism of the investigated Gerber half-joints. It is found that the load-bearing capacity is negligibly reduced (<2%) by the corrosion penetration at the current date (53 years from the construction) and moderately decreases (around 10%) at 100 years of service life. NLFEA outcomes are finally compared to simplified formulations based on strut-and-tie models and cross-sectional analyses to estimate discrepancies resulting from different levels of approximation, as suggested by modern design codes.

KEYWORDS
concrete bridges, corrosion, dapped-end beams, deterioration, Gerber joint, half-joint, nonlinear finite element analysis, numerical analysis, strut-and-tie model

1 | INTRODUCTION

Today, one of the primary concerns regarding our infrastructure network is the degradation of reinforced concrete (RC) and prestressed concrete (PC) bridges associated with steel corrosion.[1] In many European countries like Italy, Spain, France, and Portugal, the use of structural concrete has soared after World War II, especially in the 1960s and 1970s.[2] Since several bridges have a service life approaching or even exceeding 50 years, they are experiencing damage phenomena[3,4] and require careful inspection,[5] monitoring[6] and analysis for their structural safety assessment.[7] The lack of periodic and systematic inspection and maintenance plans over the last decades is likely due to the limited knowledge on durability issues of concrete structures. Unfortunately, the importance and severity of these durability issues have been highlighted by recent collapses: in Italy, only in the past 10 years, we count 15 bridge failures, 52 deaths, and 38 injuries mainly related to aging of concrete bridge structures.[8]

A peculiar connection frequently adopted in the last century for concrete bridge decks, especially road overpasses, is the Gerber half-joint,[9–11] also called dapped-end beam[12,13] or Gerber saddle.[14,15] This configuration, firstly introduced by the German engineer Heinrich Gottfried Gerber, allows the construction of suspended beams, and has some inherent advantages related to the speed of construction and to the statically determinate scheme, which is insensitive to differential settlements and thermal variations (unlike multi-span continuous girder bridges). However, Gerber half-joints are no longer used today and are considered critical elements of the existing infrastructure network because of problems related to their maintenance and durability. They have indeed shown critical issues related to possible brittle shear failure in the half-joint,[16] defective leakage of chloride-rich water with localization of material deterioration (reinforcement corrosion) in the protruding nib,[17] difficulty of visual inspection and defect detection by means of non-destructive tests. The collapse of a section of the de la Concorde Overpass in Quebec, Canada, in 2006,[18] and the more recent collapse of the Annone Brianza overpass in Italy in 2016[19] occurred in an exceptional, sudden manner, and revealed the inherent vulnerability of these kinds of concrete half-joint bridges. Moreover, in some cases the original design drawings of these elements might be unavailable, and the actual reinforcement arrangement is quite difficult to reconstruct through *in situ* tests (e.g., rebar locator, radargrams, and endoscopies) due to the significant concentration of reinforcement in relatively narrow regions of the half-joint. Guidelines and recommendations for the safety assessment of these elements are scarce and not universally recognized, as reinforcement layouts and design assumptions vary from country to country.

Previous literature studies have presented numerical analyses of deteriorated Gerber half-joints.[20–23] However, to the authors' best knowledge, no parametric study was conducted on bridge decks with half-joints while taking material deterioration into account on the basis of *in situ* experimental measurements to quantify model uncertainties related to: (i) modeling approach, involving different dimensions of the finite element model (2D and 3D), software, solvers, and implemented nonlinear concrete material model; (ii) shrinkage and creep formulation in the nonlinear finite element analyses (NLFEAs); (iii) effect of the transverse diaphragm in the section above the pier. To fill these research gaps, this paper presents advanced numerical models for simulating the structural behavior up to collapse of Gerber half-joints belonging to a real case study of highway overpasses. More specifically, this paper deals with the durability analysis and safety assessment of deteriorated Gerber half-joints belonging to a set of 50-year-old road overpasses of the A20 highway in the province of Messina, Italy. An extensive *in situ* test campaign is conducted to characterize the mechanical properties of concrete and steel materials. Based on these experimental findings, a parametric NLFEA of a portion of the bridge deck is performed to evaluate the structural behavior of these Gerber half-joints by comparing various modeling assumptions.

Material deterioration and corrosion phenomena have also been identified and quantified from the experimental campaign. Visual inspection has revealed a state of homogeneous (uniform) carbonation-induced corrosion on the steel reinforcement, with average mass losses on extracted steel bars of around 4% and average carbonation depths around twice the concrete cover. Therefore, advanced numerical models are used here for simulating the collapse behavior of Gerber half-joints, taking material deterioration into account. To this aim, NLFEAs are extended to investigate the influence of corrosion on the nonlinear response of the studied Gerber half-joints. A simplified quadratic corrosion propagation model is proposed in this work, for the first time, and is calibrated on *in situ* test results, combining carbonation depths identified from the experimental campaign with actual mass losses measured on steel bars extracted from the road overpasses. This model can be useful to extrapolate the corrosion attack depth for future times based on experimental findings at the current date, which can be useful for bridge management companies to identify critical portions of the pertinent infrastructure network and to rationally plan retrofitting actions in a timely and precise manner. This time-dependent corrosion model is incorporated in the NLFEA to investigate the variation of the load-bearing capacity and failure mechanism of Gerber half-joints associated with steel corrosion. Results from NLFEA on both uncorroded and corroded structures are finally compared to simplified formulations based on strut-and-tie models (STM) and sectional analysis to evaluate discrepancies resulting from different levels of approximation, in line with modern design codes.

2 | ROAD OVERPASSES WITH GERBER HALF-JOINTS

This paper investigates the structural behavior of Gerber half-joints belonging to a family of 18 road overpasses on the A20 highway Messina-Palermo, located near the municipalities of Rometta and Barcellona P.G., constructed in the early 1970s with a Niagara-type Gerber static scheme shown in Figure 1. The PC deck is composed of a central (suspended) span 31.0 m long, and two lateral (symmetric) cantilever spans 29.0 m long. Suspended and cantilever spans have complementary dapped ends that are connected by Gerber half-joints.

Although all the analyzed overpasses have the same scheme and span lengths, the deck of the 18 structures is formed by a number of I-shaped post-tensioned PC girders variable from 3 to 8 and corresponding to widths ranging from 6.50 m to 17.00 m, respectively. The most recurrent deck configuration (observed in 12 out of the 18 analyzed overpasses) has five girders and a total width of 10.0 m and is illustrated in Figure 2. The PC girders have variable height from 1.30 m (at the abutments) to 1.70 m (near the pier and constant along the central span) and mutually collaborate transversally through six and five cast-*in situ* RC diaphragms (rectangular section with base width of 20 or 30 cm) for the cantilever and the suspended span, respectively, and a 16 cm thick RC slab. As to the steel reinforcement arrangement, each girder has 6 + 6Ø10 longitudinal bars in the top flange and in the web, and 11Ø10 in the bottom flange. The transverse reinforcement consists of Ø12/15 cm and Ø10/30 cm for the cantilever spans and central span, respectively.

As shown in Figure 3, the prestressing cables have a parabolic profile and are composed of cold-drawn Ø7 steel wires. In the cantilever spans there are four distinct cables: cables labeled 1, 2, and 3 are made of 32 wires and are anchored at the half-joint, whereas cable 4 (located in the upper portion) is made of 42 wires and is anchored at the abutment; in the suspended span there are three cables made of 32 wires. The reinforcement arrangement in the half-joint is illustrated in Figure 3 and consists of hangers 2Ø24, diagonal bars 4Ø24, and longitudinal (top and bottom) steel bars 6Ø24 properly

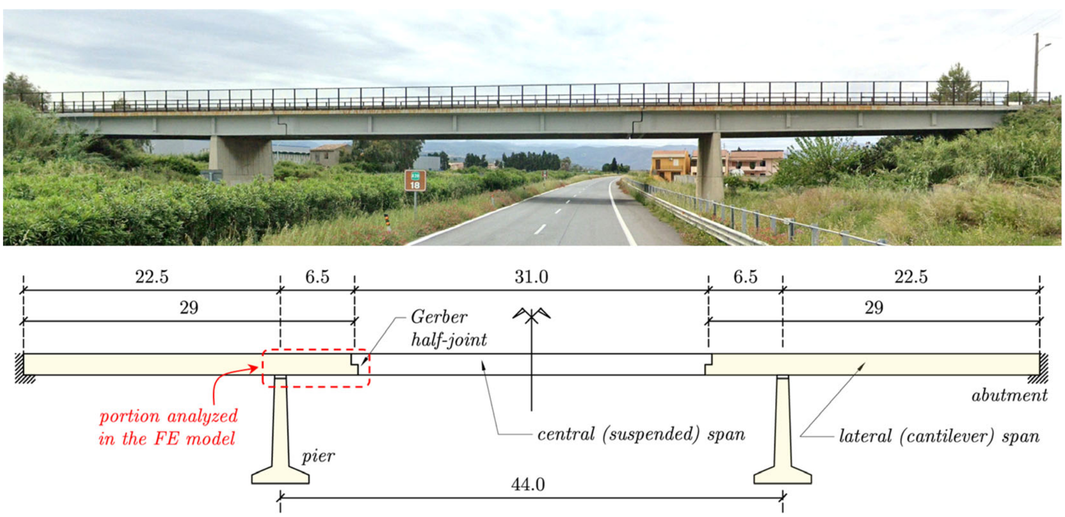

FIGURE 1 Photograph of a typical road overpass (top) and pertinent Niagara-type Gerber static scheme (bottom) with units in (m).

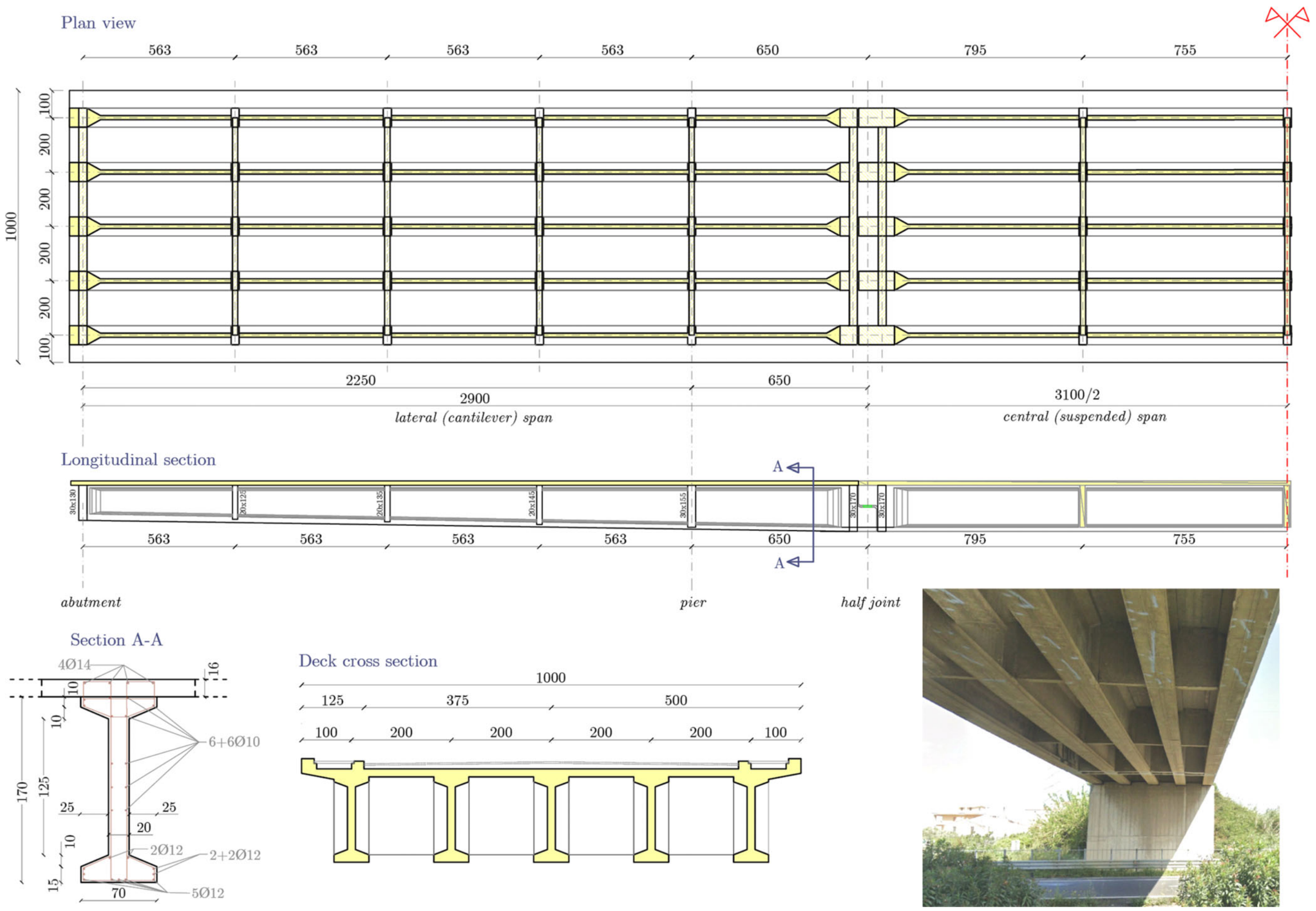

FIGURE 2 Drawings of the bridge deck with five girders, measures in (cm): Plan view (top), longitudinal section of half deck (middle), girder cross section and cross section of the entire deck along with a photograph of the deck soffit (bottom).

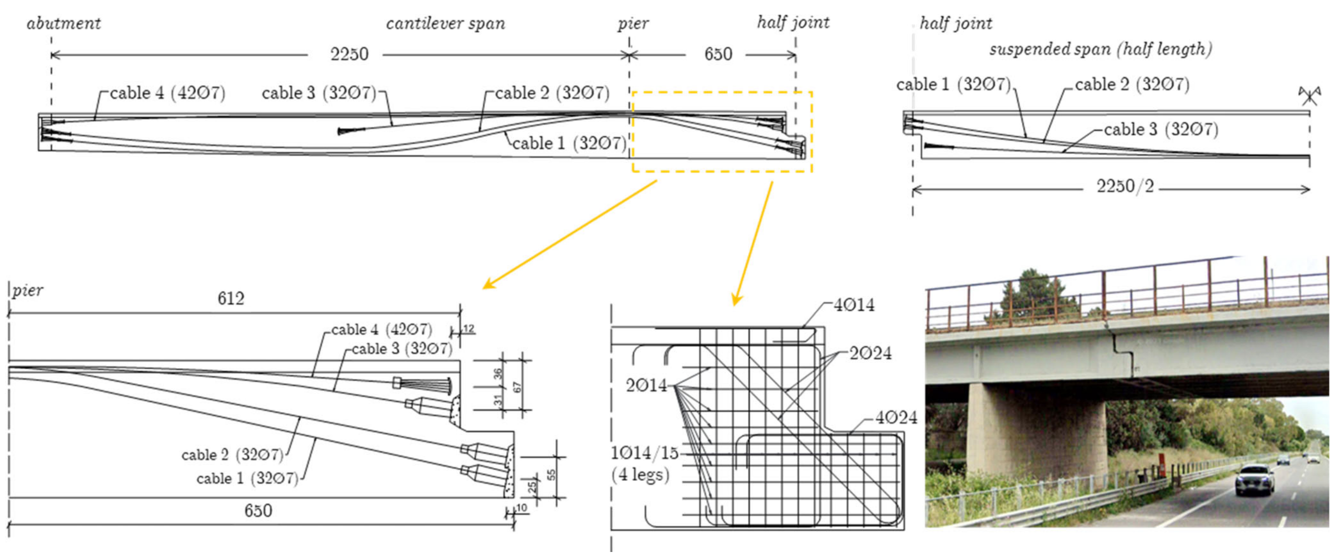

FIGURE 3 Prestressing cables profile and arrangement of longitudinal and transversal steel reinforcement bars in the Gerber half joint reproduced from original drawings, measures in (cm).

anchored, stirrups, and longitudinal skin reinforcement Ø14/15 cm. The RC slab is reinforced with 4Ø14 longitudinal bars in the central part (over the I-shaped girder flange) and 6Ø8 longitudinal bars (top and bottom) at either external side of the deck, plus Ø10/25 cm horizontal bars for the entire slab width.

3 | *IN SITU* EXPERIMENTAL CAMPAIGN

A broad experimental campaign for the mechanical characterization of concrete and steel material properties and for the identification of the material degradation and corrosion phenomena has been executed. These experimental findings are used to calibrate the nonlinear FE model illustrated in the following section. The archival survey has revealed that the 18 overpasses of the investigated case study can be divided into two distinct batches, namely batch 1 (including 7 overpasses) and batch 2 (including 11 overpasses). These two batches, placed one after the other along the investigated highway network, were constructed by two independent construction companies, using different concrete batching plants and slightly different materials. This is why, in the interpretation of the experimental campaign performed on the overpasses, in this paper statistical analysis is performed with reference to a single batch for the sake of brevity (batch 1). Of course, the methods presented in this work (parametric NLFEA and related corrosion model) are general and could be easily extended to the other batch by appropriate modification of the material parameters.

3.1 | Experimental characterization of concrete material properties

The concrete strength has been determined through *in situ* destructive and non-destructive techniques, including SonReb tests (i.e., ultrasonic pulse velocity tests combined with Schmidt rebound hammer tests[24,25]), pull-out tests[26] and extraction of cores for subsequent compression tests in laboratory,[27] for a total of 151 tests on the PC girders, and 87 tests on the RC slabs and diaphragms. After preliminarily excluding possible outliers lying outside the interval defined by Tukey[28] to obtain a more homogeneous and reliable group of test results for statistical inference, the values of mean μ and standard deviation σ of the concrete cylindrical compressive strength f_c resulting from the tests are listed in Table 1. According to the obtained values, the test type does not affect the resulting concrete strength significantly, which confirms the reliability of the non-destructive tests. The concrete strength class in PC girders is different from that observed in RC slabs and diaphragms, as reasonably expected. To reflect the experimental measurements, in the subsequent numerical analyses, two different classes of concrete are adopted, one for the slabs and diaphragms and another for the girders. Moreover, a relatively high statistical dispersion is noted in the concrete of RC slabs and diaphragms, with coefficient of variations (CoVs) around 29% compared to that of PC girders that is around 16%.

3.2 | Experimental identification of material deterioration and corrosion phenomena

During visual inspection, corrosion of steel bars on the external sides of the RC slab (edges and bottom face) and corrosion of skin reinforcement and stirrups in the half joint were observed; see Figure 4. Therefore, carbonation tests and chloride content tests were planned to identify the corrosion initiation phase and to quantify the type of corrosion. Additionally, extraction of steel reinforcing bars for the determination of their mechanical properties has made it possible to evaluate mass loss (compared to the original diameter reported in the executive drawings) by gravimetric analysis, which is useful to quantify the actual corrosion effect.

Carbonation depth x_{CO2} has been determined on 43 concrete samples: according to UNI EN 14630:2007 provisions, a phenolphthalein solution is sprayed soon after the extraction of concrete cores, and chromatic variations ascribed to different pH levels are measured to identify the depassivation front.[5] The experimental distribution of x_{CO2} is plotted in the histogram of Figure 5 (left) and is roughly fitted by some probability density functions (PDFs) through the maximum likelihood

TABLE 1 Mean μ and standard deviation σ of concrete cylindrical compressive strength f_c (MPa) identified via various tests.

		Type of test			
Structural element	Statistical value	SonReb	Pull-out	Cores	All exp data
PC girders	μ	29.6	27.3	25.5	27.3
	σ	3.14	4.06	5.41	4.19
RC slabs and diaphragms	μ	17.8	13.2	17.7	15.4
	σ	4.67	2.98	4.75	4.29

Abbreviations: PC, prestressed concrete; RC, reinforced concrete.

FIGURE 4 Corrosion state localized in the reinforced concrete (RC) slabs (left) and in the half-joints (right) of the analyzed road overpasses.

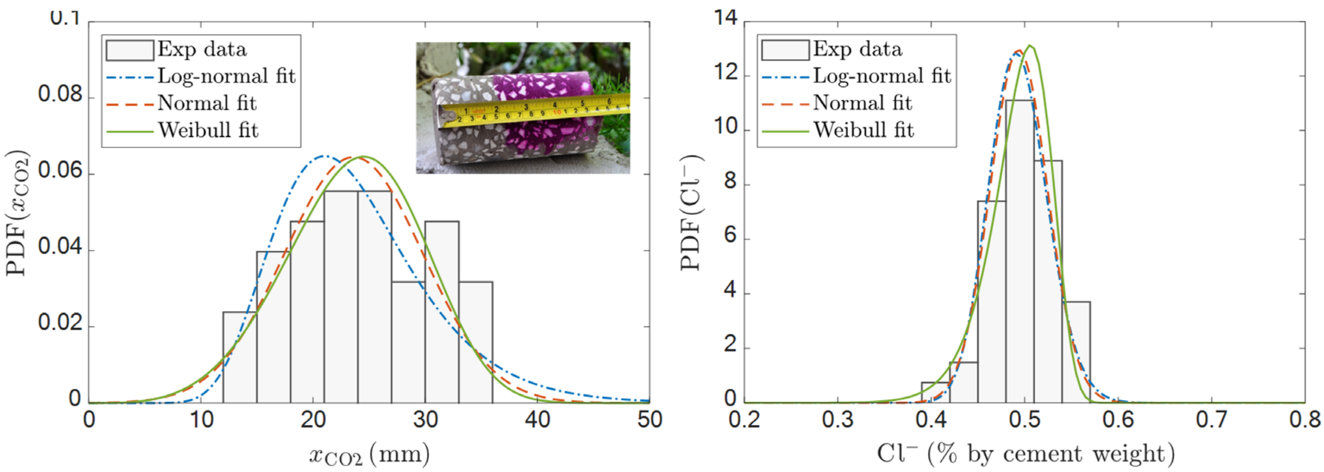

FIGURE 5 Carbonation depths (left) and chloride content (right) with probability distribution fitting.

estimation (MLE) method. The range of x_{CO2} is variable from 13 to 35 mm, with a mean value equal to 23.6 mm. This dispersion is ascribed to multiple factors, like the different environmental exposure and the heterogeneous porosity of various concrete samples, reflected in the high CoV of the compressive strengths already noted in Table 1. It is worth noting that the concrete cover identified from pachometric tests is, on average, 15 mm; consequently, the shallower layers of steel bars are, after 53 years of service life, surrounded by carbonated concrete.

In addition to carbonation depths, the content of chloride ions Cl$^-$ has been determined by analyzing 45 small samples of concrete at two different depths, namely in a shallower range of 0–1 cm and at a deeper interval of 5–6 cm, so as to reconstruct a possible profile of chloride diffusion across the concrete depth. Chemical tests have revealed negligible differences in the two analyzed intervals, which suggest that no ongoing diffusion process is taking place, and that the chloride content is likely related to an initial contamination of concrete during on-site mixing. It is worth noting that deicing salts were never used in these overpasses due to the temperate climate conditions. As shown in Figure 5 (right), the values of Cl$^-$ are tightly concentrated around the mean value of 0.5% and are well fitted by a normal distribution. The obtained values are below typically critical contents of conventional Portland cements[29]: these results, along with the direct observation of the actual steel bars extracted from the structure that appeared visibly corroded but without localized reduction of their cross section, lead us to exclude the presence of pitting corrosion and to justify the hypothesis of uniform corrosion in the numerical simulation discussed in the sequel of the manuscript.

The extraction of 62 steel bar portions from girders, slabs, abutments, and piers was useful not only to determine the mechanical properties (as described in the next subsection) but also to calculate the average mass loss Δm (or corrosion degree with respect to the original mass) through gravimetric analysis as per American Society for Testing and Materials (ASTM) guidelines[30]:

$$\Delta m = \frac{m_o - m^*}{m_o}, \tag{1}$$

where m_o and m^* represent the mass of the uncorroded and corroded bar, respectively.[7] The corrosion attack penetration in terms of Δm is quantified in the histogram of Figure 6 (left), whose statistical trend is reasonably fitted by an exponential distribution or a half-normal distribution: in 24 out of the 62 samples $\Delta m = 0$, while in 26 samples the measured mass loss exceeded 3%, with an average value equal to 4.2% and peaks up to around 30%. These values, measured after 53 years of service life of the road overpasses and combined with the carbonation depths discussed above, are important ingredients for calibrating a simplified time-dependent corrosion proposed in the following sections.

The average corrosion penetration P_{corr} can be determined indirectly from the mass loss Δm[31,32] as follows:

$$P_{corr} = \frac{\phi_0}{\alpha}\left(1 - \sqrt{1 - \Delta m}\right), \tag{2}$$

where ϕ_0 is the uncorroded diameter and the factor $\alpha = 2$ for homogeneous (uniform) corrosion.[33] It is worth noting that the uncorroded bar diameter ϕ_0 is represented by the nominal diameter reported in the executive drawings in the region of extraction of the steel sample. The Equation (2) is based on an equivalent diameter ϕ^* at a given time t, which is calculated by assuming a circular cross section after corrosion[34,35] according to Figure 6 (right):

$$\phi^* = \phi_0 \times (1 - \alpha \times P_{corr}). \tag{3}$$

The Equations (2) and (3) are applicable not only to uniform corrosion ($\alpha = 2$) but also to pitting corrosion by assuming a pitting factor α in the range of 5–10,[36] although in the present case study pitting corrosion is deemed not relevant.

3.3 | Experimental characterization of steel material properties

After performing the gravimetric analysis, the steel bar samples are tested in the laboratory to determine their effective tensile properties referred to the equivalent cross-section area of the corroded bar $A^* = \pi\phi^{*2}/4$, namely yield stress f_y, ultimate stress f_u, and ultimate strain ε_{su}, whose distribution is illustrated in Figure 7 along with some proposals of probability distribution fitting. A relatively high dispersion is noted in the tensile properties, especially with regard to the ultimate strains. The results refer to all bar diameters (from 8 to 24 mm)

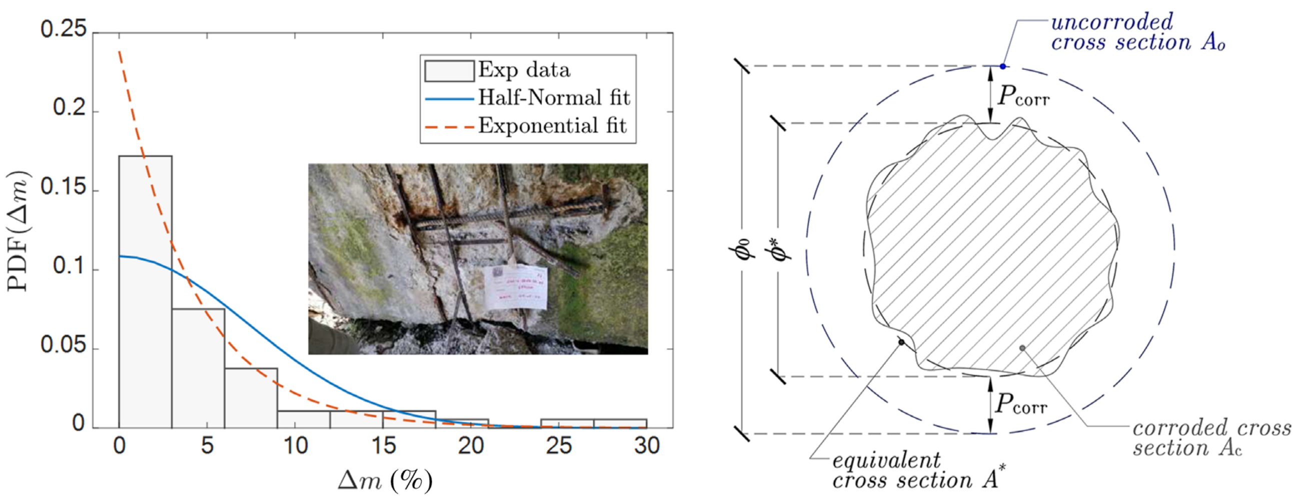

FIGURE 6 Average mass loss determined by gravimetric analysis on 62 portions of steel bars extracted from the road overpasses with probability distribution fitting (left) and evaluation of equivalent corroded area under the assumption of uniform corrosion (right).

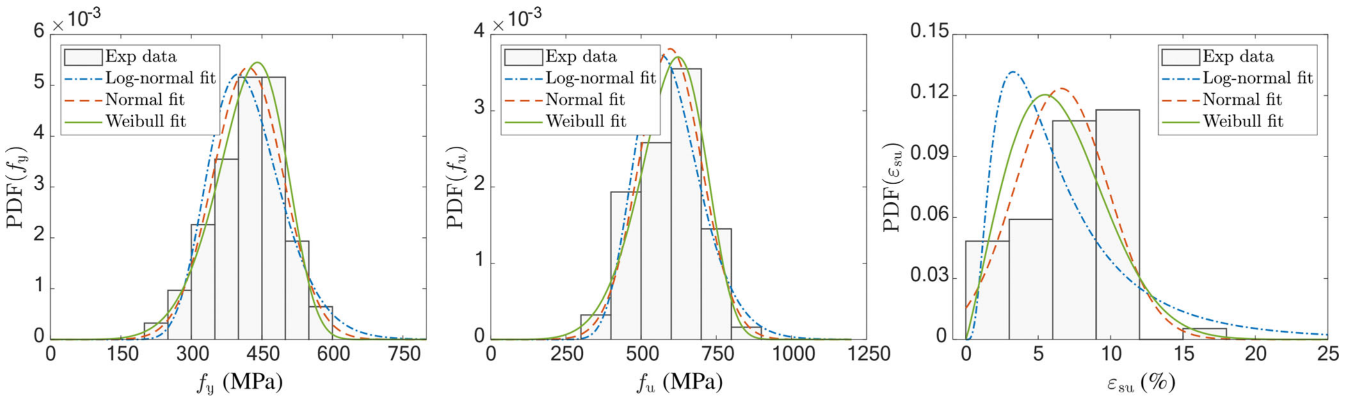

FIGURE 7 Yield stress (left), ultimate stress (center) and ultimate strain (right) determined on 62 portions of steel bars extracted from the road overpasses with probability distribution fitting.

TABLE 2 Mean μ and standard deviation σ of mechanical characteristics of steel bars extracted from the road overpasses.

	f_y (MPa)		f_t (MPa)		ε_{su} (%)	
Steel bars	μ	σ	μ	σ	μ	σ
With $\Delta m < 4\%$ (37 samples)	431	73	611	99	7.1	3.4
With $\Delta m \geq 4\%$ (25 samples)	406	75	576	111	5.8	2.9
All data (62 samples)	421	75	597	105	6.6	3.2

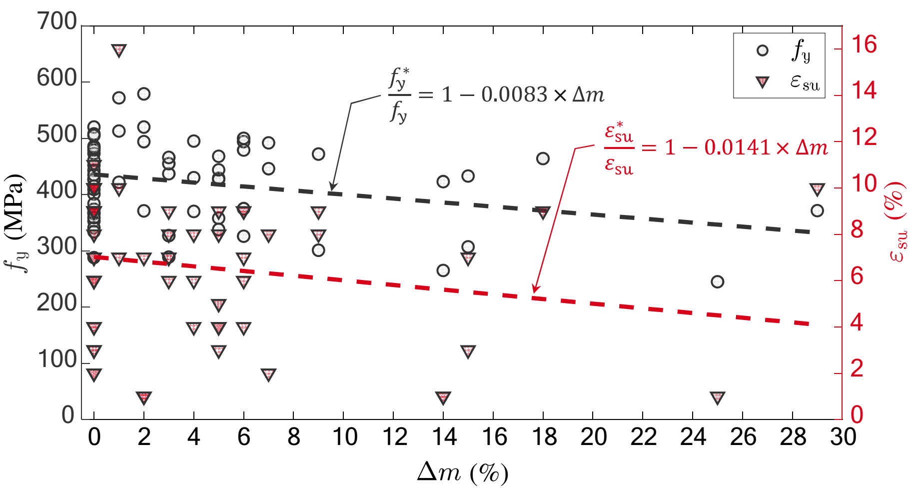

FIGURE 8 Variation of yield stress and ultimate strain with average mass loss identified from experimental tests.

because similar trends are noted by analyzing single diameters individually; therefore, they have been merged to have a statistically meaningful population for more reliable estimates. The mean and standard deviation values are listed in Table 2 by separating the 37 steel bars having $\Delta m < 4\%$, that is, characterized by negligible mass loss, from the remaining 25 samples with $\Delta m \geq 4\%$, so as to identify possible influences of the corrosion on the mechanical properties of steel reinforcement.

It seems that the corrosion has a marginal influence on the value of yield and ultimate stress, with reductions of f_y and f_u, on average, in the order of 5%, and has a moderate impact on the ductility, with ultimate strain values ε_{su} on corroded bars that are, on average, 18% lower than those of the uncorroded bars. To further analyze these results, in the scatter plot of Figure 8 we correlate the experimentally detected values of f_y and ε_{su} with the measured Δm of the corresponding steel bars extracted: the dashed trendlines roughly fitted to such experimental datapoints can be critically compared to linearly decaying formulations proposed in the literature[37–40] for predicting the reduction of yield stress

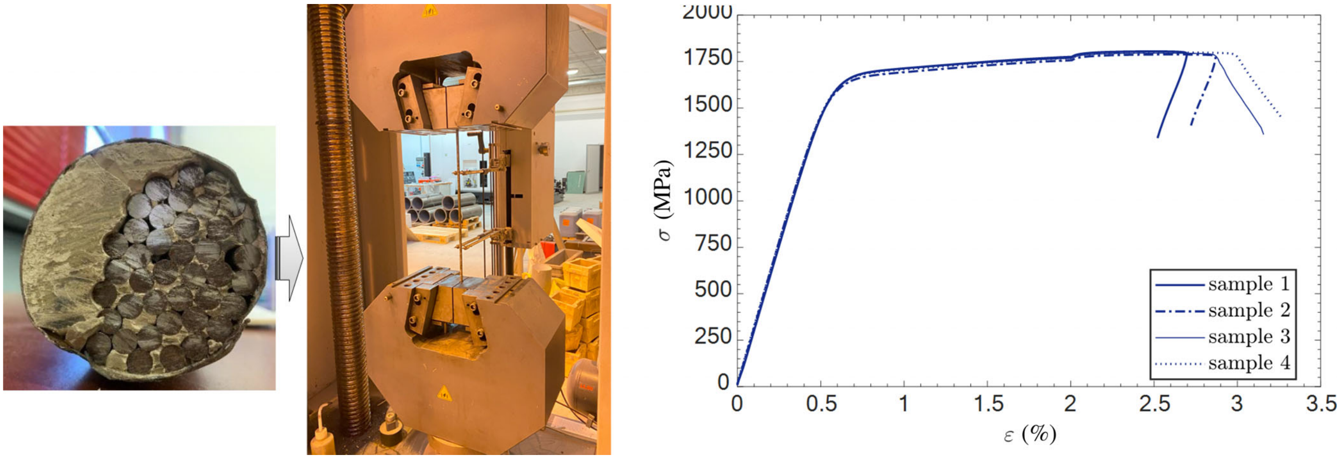

FIGURE 9 Tensile tests on prestressing wires extracted from cables of a dismantled viaduct having comparable age and environmental exposure as the analyzed road overpasses.

and ultimate strain with Δm through empirical angular coefficients β_{fy} and $\beta_{\varepsilon_{\mathrm{su}}}$, respectively:

$$\frac{f_{\mathrm{y}}^{*}}{f_{\mathrm{y}}}=1-\beta_{\mathrm{fy}}\times\Delta m;\quad \frac{\varepsilon_{\mathrm{su}}^{*}}{\varepsilon_{\mathrm{su}}}=1-\beta_{\varepsilon_{\mathrm{su}}}\times\Delta m. \tag{4}$$

When performing this comparison, it should be noted that the tested samples are naturally corroded steel bars embedded in concrete undergoing uniform corrosion in a CO_2-rich environment due to the presence of an electrical plant and a petrol-chemical transformation farm in the nearby, and that the considered concrete was possibly affected by issues in the casting phase, like an inadequate compaction and heterogeneous water/binder ratios, especially in the RC slabs and diaphragms as confirmed by the poor and dispersed mechanical strengths.

It is also important to characterize the mechanical properties of the prestressing steel. The extraction of Ø7 strands from the posttensioned cables of the PC girders was deemed too invasive and was avoided; however, the characterization of the prestressing steel of the road overpasses was performed indirectly. It was indeed possible to extract Ø7 prestressing wires from posttensioned cables of another dismantled viaduct belonging to the same A20 highway as the road overpasses and constructed in the same years (early 1970s), thus having comparable age and environmental exposure. These wires are tested in the structural laboratory of the University of Messina, and relevant results are shown in Figure 9: the steel strands exhibit a distinct bilinear stress–strain relationship, with a mean value of 0.1% proof-stress $f_{\mathrm{p}(0.1)}$ equal to 1648 MPa and a mean value of tensile strength $f_{\mathrm{pu}}=1797$ MPa, which are in reasonable agreement with values reported in other literature papers for bridges realized in southern Italy in the 1970s.[41]

4 | PARAMETRIC NLFEA ON UNCORRODED GERBER HALF-JOINTS

As can be noted by the executive drawings in Figures 2 and 3, the peculiarities of the analyzed PC half-joint bridges are: (1) oversized hangers and diagonal reinforcement bars in the dapped end; (2) inadequate concrete compressed area in the section above the pier subject to negative bending moment. Based on the experimental findings discussed in the previous section, a parametric 2D and 3D NLFEA is performed. A portion of the bridge deck extending from the Gerber half-joint to the section above the pier is modeled (see again the sketch in Figure 1) with the aim to quantify model uncertainties related to: (i) modeling approach, involving different dimensions of the FE model (2D and 3D), software, solvers, and implemented nonlinear concrete material model; (ii) shrinkage and creep formulation in the NLFEAs; (iii) effect of the transverse diaphragm in the section above the pier. Four models labeled M1–M4 have been comparatively considered, whose characteristics are summarized in Table 3. Corrosion effects are ignored in these preliminary parametric analyses because NLFEAs are extended in the next section to incorporate corrosion-induced material degradation.

4.1 | 2D NLFEAs by VecTor2 software

2D NLFEAs are performed by means of the VecTor2 software.[42] This software implements the well-established Modified Compression Field Theory (MCFT)[43] and the Disturbed Stress Field Model (DSFM)[44] developed at the University of Toronto in the last decades. The software is equipped with a pre-processor suitable for preparing a bidimensional FE model: the model of the Gerber half-joint analyzed in this work is shown in Figure 10. Concrete regions have a constant thickness and are distinguished by different colors. They are modeled through triangular elements with two degree of freedoms per node. The uniaxial concrete stress–strain laws in compression for slab ($f_c = 15.4$ MPa) and girders ($f_c = 27.3$ MPa), respectively, are modeled using the analytical curve proposed by Mander et al.[45] (Figure 11, left), while the concrete cracked behavior is considered by reducing the constitutive curve through a compression softening coefficient that is a function of the principal tensile strain field.[43] The nonlinear constitutive model also accounts for the tension stiffening effect in the cracked concrete around the steel bar by incorporating the influence of reinforcement bond characteristics through the formulation proposed by Bentz.[46]

Vertical steel bars of all concrete regions are smeared. Longitudinal and inclined steel bars, as well as posttensioned cables, are instead modeled by means of two-node truss elements embedded in the concrete elements. The

TABLE 3 Characteristics of the finite element models considered in the parametric analysis.

Model ID	FE model dimension	Shrinkage and creep formulation[a]	Transverse diaphragm in the section above the pier
M1	2D and 3D	Explicit	Neglected
M2	2D and 3D	Implicit	Neglected
M3	2D and 3D	Explicit	Included
M4	2D and 3D	Implicit	Included

[a]Explicit: long-term deformation phenomena applied as isotropic contraction to all concrete finite elements; implicit: stress losses applied to prestressing cables based on shrinkage and creep deformations in surrounding concrete.

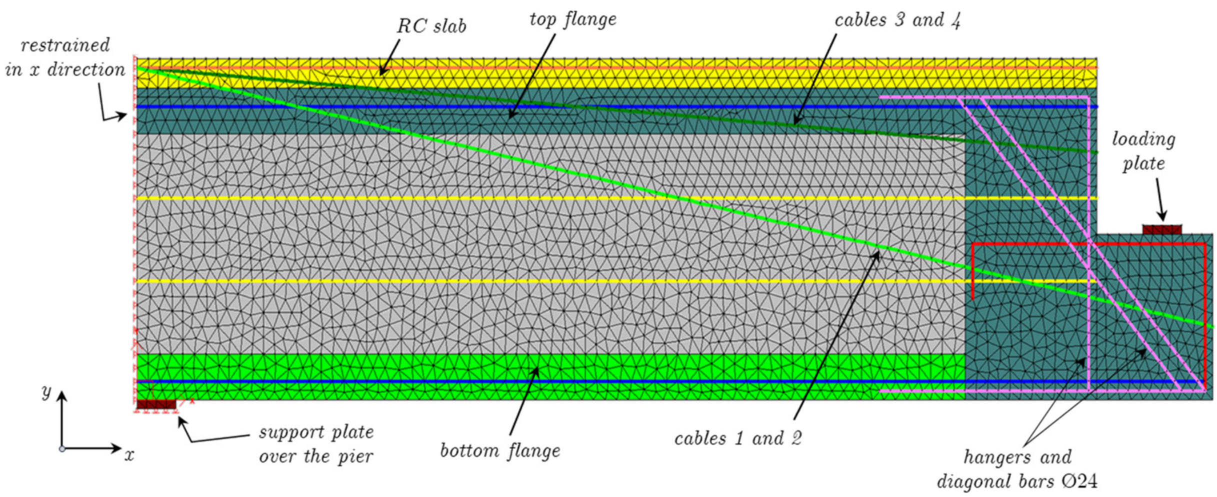

FIGURE 10 2D nonlinear finite element model of the Gerber half-joint through the VecTor2 software[42], by using triangular elements for concrete and discrete embedded truss elements (combined with smeared reinforcement) for steel reinforcing bars and prestressing cables. RC, reinforced concrete.

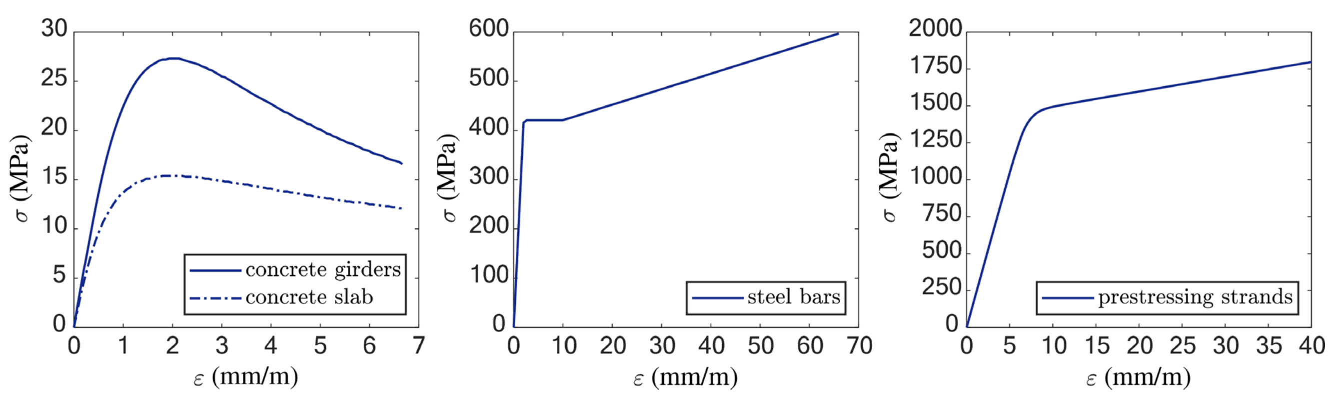

FIGURE 11 Stress–strain relations adopted in the 2D FE model for concrete (left), steel bars (center), and prestressing strands (right).

constitutive behavior of steel bars is modeled by means of a tri-linear curve that incorporates a hardening branch after the yielding plateau (Figure 11, center), while the Ramsberg and Osgood[47] formulation is adopted for the prestressing steel (Figure 11, right). The mechanical properties of steel are calibrated upon experimental mean values ($f_y = 421$ MPa, $f_t = 597$ MPa, $\varepsilon_{su} = 6.6\%$, $f_{p(0.1)} = 1648$ MPa, $f_{pu} = 1797$ MPa). In order to simplify the model while keeping accuracy, the four prestressing cables (Figure 3) are coupled in two pairs of truss elements: cables 1 and 2, having 32 wires each, follow a straight profile starting from the top slab and ending in the protruding nib of the half-joint, thus they are grouped into a single truss element; similarly, cables 3 and 4, having 32 and 42 wires, respectively, follow a sub-horizontal path at the level of the top slab, thus they are also grouped into a single truss element. The final mesh consists of 5195 triangular elements and 896 truss elements.

Prestress force in the cables is applied through an initial prestrain ($\Delta_{\varepsilon p}$) in the material associated with the truss elements, so that the resulting force in the cable at the initial stage of the analysis is equal to $E_{sp} \times \Delta_{\varepsilon p} \times A_p$, being E_{sp} the elastic modulus of steel assumed equal to 200 GPa and A_p the total area of the cables considered. The prestrain value in the cable material is also influenced by shrinkage and creep deformations that are modeled in two different ways: *explicitly* and *implicitly* (Table 3). In the first case, shrinkage and creep deformations are considered by means of a specific load case through an initial prestrain value (Δ_{ε_c}) applied to all concrete elements; therefore, the initial strain of the cables is estimated without considering shrinkage and creep because the corresponding prestress losses are taken into account in an *explicit* manner. In the second case, shrinkage and creep deformations are, instead, included in the calculation of the initial strain of the cables ($\Delta_{\varepsilon p}$), therefore they are not applied to concrete elements because they are considered *implicitly* in the prestress value applied to the cables.

Self-weight is considered as a volume load applied to all concrete elements at the first step of the analysis, then a unitary displacement is applied to the nose of the half-joint and is amplified at each step (push-down scheme), performing a displacement-control nonlinear analysis up to the structural collapse. The software adopts a secant-stiffness approach to satisfy convergence criteria at each step of the analysis. To avoid localized concrete crushing, elastic steel plates with a thickness of 50 mm are modeled under the loading point and to simulate the bearing support over the pier that sustains vertical reaction forces. In addition, horizontal restraints are applied along the vertical edge of the cantilever over the pier to simulate continuity condition; thus the remaining part of the girder can be excluded by the model.

4.2 | 3D NLFEAs by ATENA software

Parametric analyses are also performed with the 3D nonlinear FE code ATENA.[48] A sketch of the model with main assumptions on element types, loading, and boundary conditions is illustrated in Figure 12. We adopt the "CC3DNonLinCementitious2" material model for concrete, which is based on an efficient three-dimensional fracture-plastic approach[49] combining tensile fracture behavior and compressive plastic behavior. For describing concrete response in tension, the fracture model relies on an orthotropic fixed smeared crack formulation based on the Rankine failure criterion with exponential softening. Concrete crushing is instead governed by the triaxial Menétrey-Willam failure surface[50] incorporated within a hardening/softening plasticity model, which describes the plasticity of concrete under multiaxial stress state in compression. The entire set of nonlinear material parameters is generated by empirical relationships[51] based on the mean compressive strength of concrete, by distinguishing girders ($f_c = 27.3$ MPa) from slabs and diaphragms ($f_c = 15.4$ MPa) to reflect the experimental strength identified from the *in situ* test campaign. A return mapping algorithm is adopted for integrating the constitutive equations with a purely incremental formulation.

Steel reinforcement bars and posttensioned cables are modeled in their actual locations through discrete truss elements embedded in the concrete elements with a perfect bond assumption, and are described by a bilinear elastic–plastic material "CCReinforcement" model whose parameters are calibrated upon experimental mean values ($f_y = 421$ MPa, $f_t = 597$ MPa, $\varepsilon_{su} = 6.6\%$, $f_{p(0.1)} = 1648$ MPa, $f_{pu} = 1797$ MPa). As can be seen in Figure 3, the anchorage lengths of the steel bars seem quite large compared to the spans involved. Since the analyzed road overpasses are in service conditions and cannot be tested, implementing a bond-slip law within the present FE model might introduce an additional source of variability in the numerical results, and was purposely avoided because of the above-mentioned reinforcement detailing configuration. Therefore, it is assumed that the length of the steel bars is sufficient to avoid anchorage failure and to justify the perfect bond assumption. In other words, it is implicitly assumed in this study that the bond stress cannot reach the value of the bond strength, as was also observed in other studies dealing with dapped-end beams in which, although the

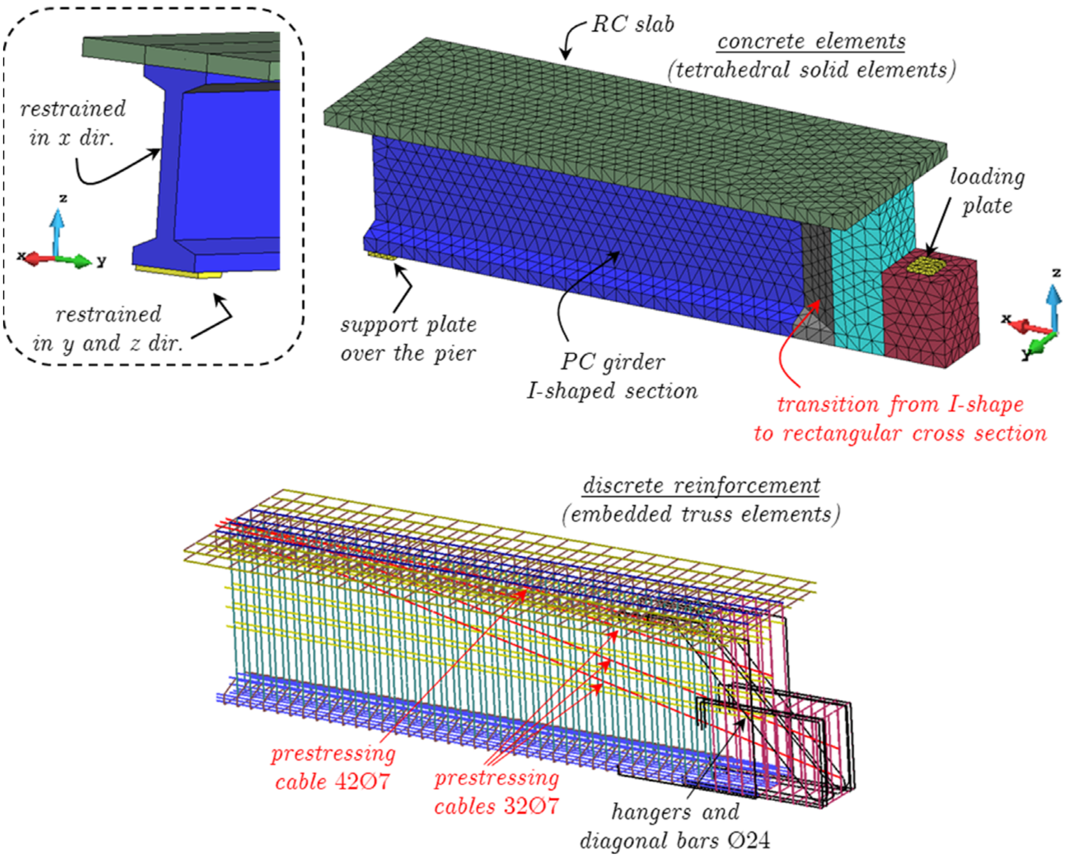

FIGURE 12 3D nonlinear finite element model of the Gerber half-joint through the ATENA software[48], by using tetrahedral elements for concrete and discrete embedded truss elements for steel reinforcing bars and prestressing cables. PC, prestressed concrete; RC, reinforced concrete.

FE model could detect anchorage failure in principle, this failure scenario was not observed.[13]

The vertical force transferred from the suspended span to the dapped end of the cantilever beam through the Gerber half-joint is distributed over a square loading plate having 300 mm side, while another rectangular plate 300 × 700 mm (with zero imposed displacement in the *y* and *z* directions) simulates the bearing support over the pier. Loading and support plates are both characterized by a linear elastic material model "CC3DElastIsotropic". Zero *x* displacement is imposed in the cross section above the pier section (face in the *yz* plane) to simulate the continuity condition along the segment of the cantilever beam not included in the model. Master–slave constraints are adopted at each concrete-plate interface. The prestressing force is applied by assigning initial strain in the truss elements that simulate the posttensioned cables through the option "Initial Strain for Reinf Line", by setting initial prestress $\sigma_{p0} = 1350\,\text{MPa}$ and relaxation losses $\Delta_{\sigma_{pr}} = 46\,\text{MPa}$ calculated according to §5.10.3 and §3.3.2 of the Eurocode 2 part 1 (EC2-1),[52] respectively. For the cable 4, which is anchored in the abutment that is beyond the portion included in the FE model, prestress loss due to friction ΔP_{μ} are taken into account according to the formulation described in §5.10.5.2 of EC2-1.[52] Assuming elastic modulus $E_p = 200\,\text{GPa}$ for the prestressing steel wires, the resulting initial strain is 0.00652 for cables 1–3, and 0.00630 for cable 4. Losses due to elastic deformation of the surrounding concrete are automatically considered in the FE model. Shrinkage and creep deformations are calculated as per §3.14 of EC2-1,[52] and are equal to $\varepsilon_{cs} = -1.68 \times 10^{-4}$ and $\varepsilon_{cc} = -4.32 \times 10^{-4}$, respectively. In the models M1 and M3, shrinkage and creep deformations are assigned through the option "Initial Strain for Volume" in the concrete finite elements, thus simulating the actual coactions arising in the concrete volume elements (*explicit* formulation). On the contrary, in the models M2 and M4, the effects of shrinkage and creep deformations are applied only as prestress losses in the prestressing cables (*implicit* formulation), by considering an additional reduction of prestress equal to $\Delta\sigma_{p,c+s} = E_p \times (\varepsilon_{cs} + \varepsilon_{cc})$, which reduces the applied initial strain to 0.00592 and 0.00570 for cables 1–3 and cable 4, respectively.

3D solid tetrahedral elements with four nodes per element (CCIsoTetra) are used for all concrete regions and for loading and support plates. After a preliminary mesh sensitivity study, 19,331 3D tetrahedra elements and 5347 embedded truss elements are used. A nonlinear solver (PARDISO) with Newton–Raphson method is used to solve the governing nonlinear equations. A multi-step nonlinear analysis is carried out: first, self-weight and service loads are applied in force-controlled mode. Self-weight is considered in the model as a force per unit volume applied to all the 3D solid tetrahedral elements representing the concrete portions, considering a specific weight of 25 kN/m^3. The service load is instead represented by the vertical reaction force transferred from the suspended span to the dapped end of the cantilever beam through the Gerber half-joint. This reaction force, which is equal to 434 kN (i.e., 330 kN of structural permanent loads plus 104 kN of superimposed dead loads, calculated on the basis of a load analysis accounting for the spacing of the girders), is applied to the model as a uniform pressure onto the above-mentioned square loading plate simulating the bearing support area. Then, a nonlinear incremental analysis (push-down) up to failure is executed in displacement-control mode by increasing the half-joint deflection until failure to simulate a progressive increase of the vertical reaction transferred by the suspended span. Two sets of NLFEAs are carried out by neglecting (M1 and M2) or including (M3 and M4) the transverse diaphragm in the section above the pier, as shown in Figure 13.

4.3 | Results of parametric analysis and discussion

Load–displacement curves obtained by 2D and 3D NLFEAs on the four analyzed models are depicted in Figure 14, while pertinent values of peak load $P_{\max}$ and displacement attained at peak load $d_{\max}$ (displacement capacity) are listed in Table 4. For clarity, the outputs of the various stages of the nonlinear analysis are highlighted with gray circles in the force–displacement curves of Figure 14: A-B represents the response to the self-weight (force-control); B-C represents the prestressing, which induces an upward movement of the dapped end (negative displacement); C-D concerns the application of service load (force-control); point D represents the beginning of the push-down analysis (displacement-control) up to failure. In the models in which long-term effects (shrinkage and creep deformations) are implemented explicitly (models M1 and M3), these phenomena are applied as isotropic contraction to all concrete finite elements immediately after point C, and do not produce any parasitic reaction. Minor differences between the two curves are observed in the prestressing branch B-C, which could be ascribed to the different geometrical assumptions of the cable locations in the 2D NLFEA in which prestressing cables are grouped in pairs. Despite the different assumptions on model geometry and concrete nonlinear material behavior, 2D and 3D NLFEAs provide comparable results. The post-peak decaying branch of the load–displacement graphs appears sharper in the 2D NLFEAs compared to the 3D NLFEAs, which can be ascribed to the different softening models of the two concrete material formulations.

An interesting aspect concerns the influence of the shrinkage and creep formulation on the load-bearing capacity of the analyzed Gerber half-joints predicted by NLFEAs: the implicit formulation, typically used in engineering practice for design and verification of PC members, leads to higher values of peak load compared to the explicit formulation. The peak load of the model M2 is indeed around 5% (for 2D NLFEA) and 10% (for 3D NLFEA) higher than that of the model M1, and the peak load of the model M4 is around 9% higher than that of the model M3 in both 2D and 3D NLFEAs. This can be explained by looking at Figure 15, where the crack width distribution at various steps of the 3D NLFEA for the two models M1 and M2 is illustrated at equal scale for comparative purposes. In the model M1, after application of prestress plus shrinkage and creep deformations of concrete, cracks develop more widely than those (almost

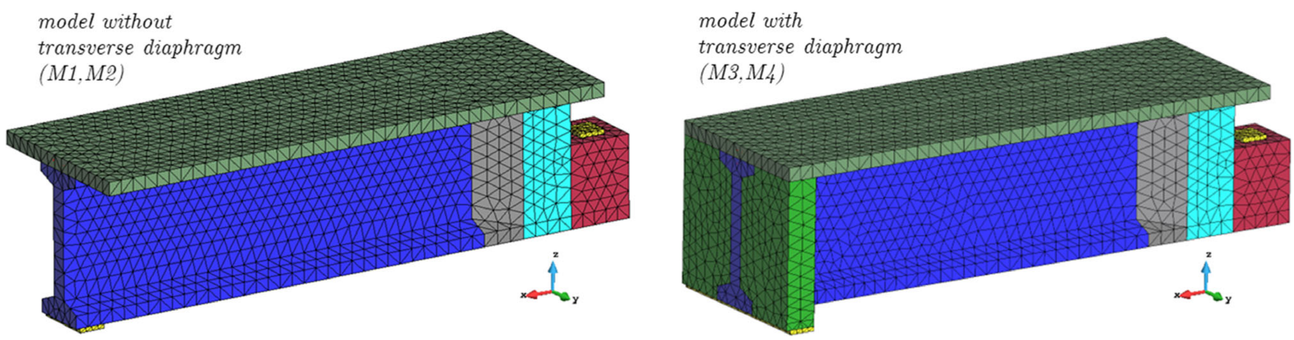

FIGURE 13 3D FE models without and with transverse diaphragm in the section above the pier.

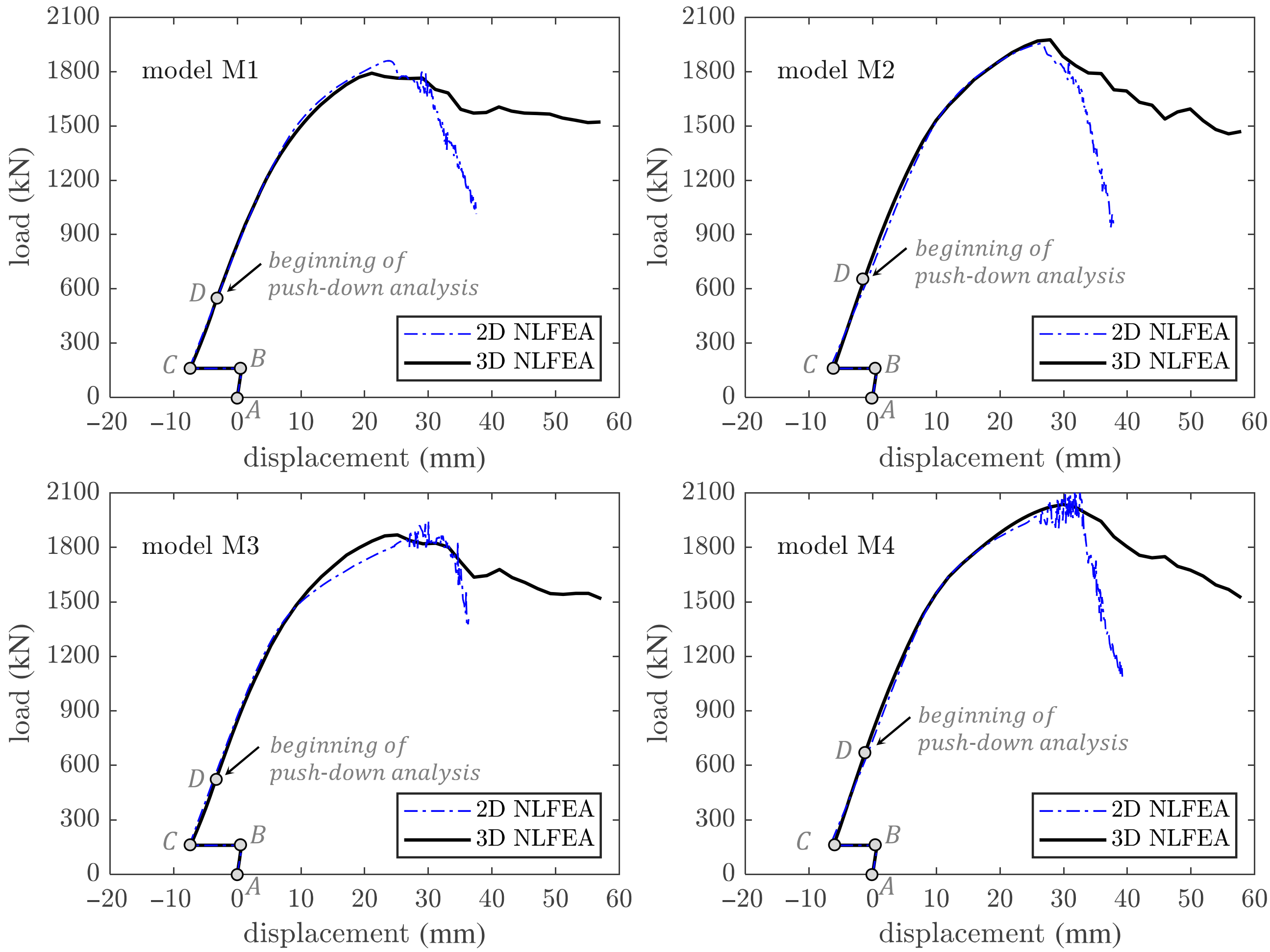

FIGURE 14 Load–displacement curves obtained by nonlinear finite element analysis (NLFEA) with different modeling assumptions.

TABLE 4 Results of nonlinear finite element analysis in terms of peak load $P_{\max}$ and displacement attained at peak load $d_{\max}$ (displacement capacity).

	2D model (VecTor2[42])		3D model (ATENA[48])	
Model ID	$P_{\max}$ (kN)	$d_{\max}$ (mm)	$P_{\max}$ (kN)	$d_{\max}$ (mm)
M1	1861	23.7	1792	21.1
M2	1957	25.6	1977	27.9
M3	1945	30.3	1869	25.1
M4	2115	30.9	2036	29.9

negligible) observed in the model M2 after application of prestress force only, whose value is reduced to account for long-term deformation phenomena of concrete implicitly. In other words, the explicit application of isotropic contractions to concrete elements gives rise to additional tensile stresses in concrete due to the perfect bond with steel reinforcement bars, especially in the region around the half-joint. This is clearly visible up to collapse, as shown in the bottom part of Figure 15 reporting the crack width distribution at peak load attainment. In both cases (M1 and M2), the failure is associated with a diffuse cracking in the top RC slab starting from the section above the pier subject to negative bending moment and spreading laterally, accompanied by concrete crushing localized in the bottom part of the girder cross section near the support, as highlighted by the equivalent plastic strains depicted in Figure 16. The crack pattern in the half-joint is relatively less pronounced in

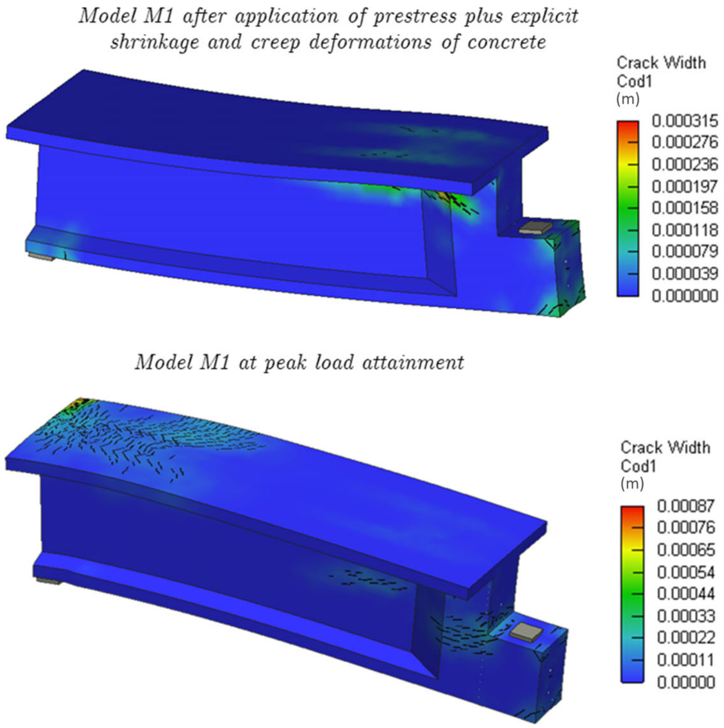

FIGURE 15 Comparison of crack width distribution between model M1 and model M2 at various steps of the 3D nonlinear finite element analysis.

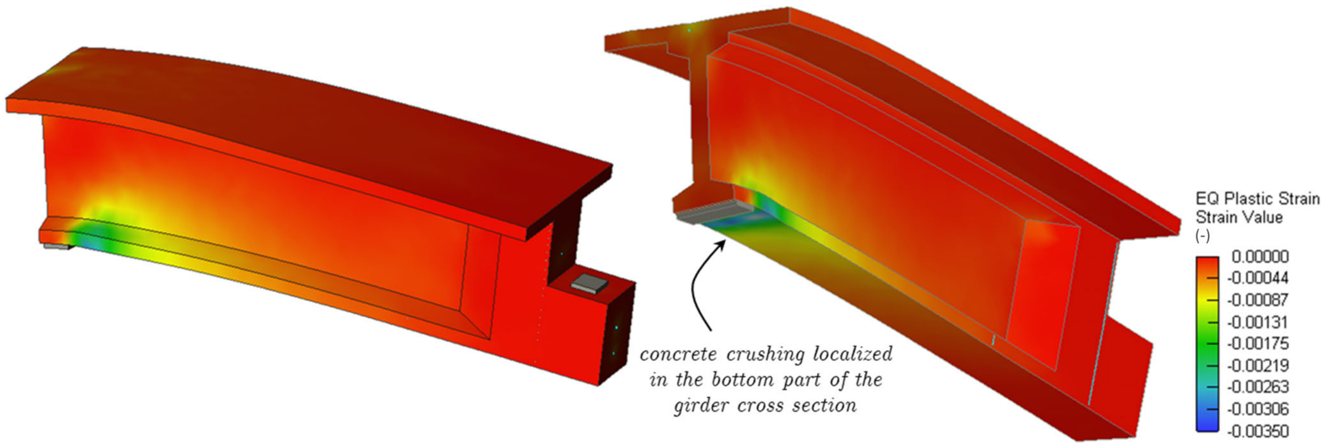

FIGURE 16 Equivalent plastic strains obtained by 3D nonlinear finite element analysis on model M2 at peak load attainment.

model M2 compared to model M1 for the reasons explained above.

In the models with transverse diaphragm (M3 and M4), the displacement capacity increases up to 25% compared to the models without transverse diaphragm; cf. again values in Table 4. As can be noted in Figure 17, the crack pattern at peak load attainment still reveals that the failure is dominated by flexural collapse near the pier section; however, the failure region in the models M3 and M4 involves a larger portion of the longitudinal element compared to that of model M1 and M2, which is reasonable as the critical section moves slightly toward the half-joint due to the stiffening effect induced by the transverse diaphragm in the section above the pier.

Similar considerations can be made for the failure mechanisms obtained by 2D NLFEAs shown in Figure 18. In this case, we additionally observe that the models M1 and M3, in which the effects of shrinkage and creep are taken into account by applying an initial prestrain value to all concrete elements, are characterized by a broad crack pattern involving almost the entire height of the girder. This approach leads to a spread crack pattern before starting the push-down analysis case and, consequently, a slightly reduced slope of the ascending

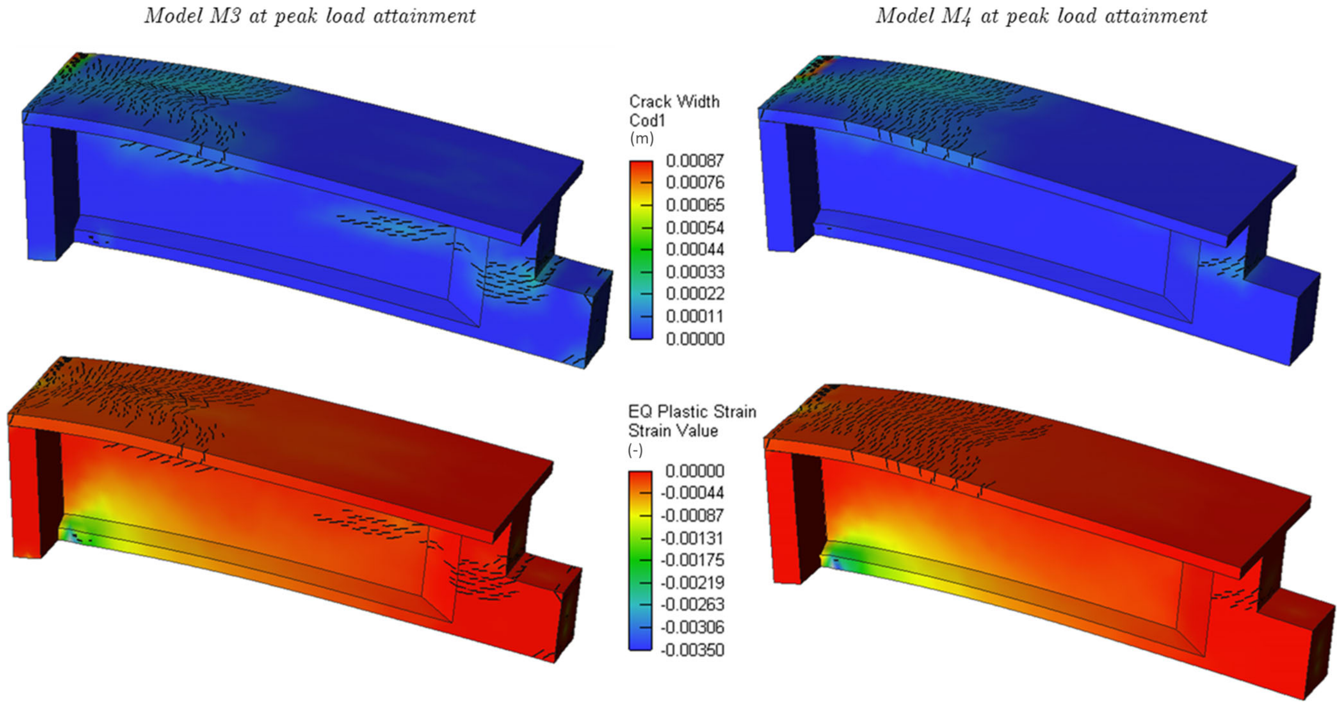

FIGURE 17 Crack widths and equivalent plastic strains obtained by 3D nonlinear finite element analysis on models M3 and M4 at peak load attainment.

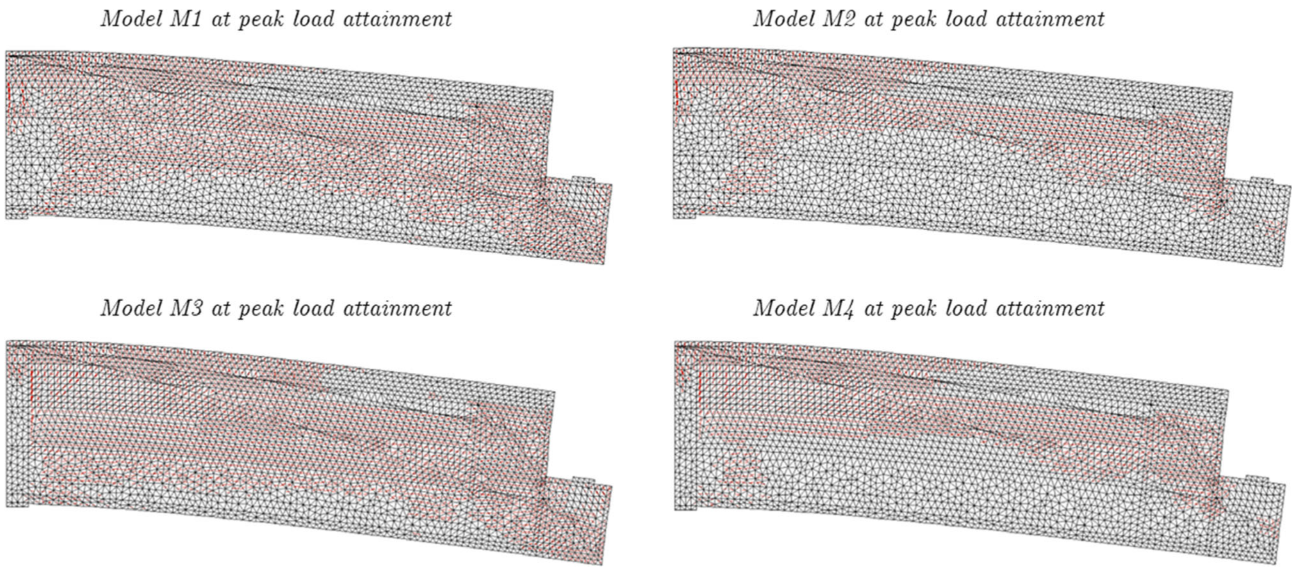

FIGURE 18 Crack pattern at failure obtained by 2D nonlinear finite element analysis on all models analyzed.

branch of the load–displacement curve for both model M1 and M3 is achieved (Figure 14).

To sum up, the critical analysis of the four models has highlighted that: (1) the collapse of the analyzed element is dominated by the flexural failure in the section above the pier while the shear in the re-entrant corner does not constitute the governing mechanism, which is due to the large quantity of hangers and diagonal steel bars in the half-joint; (2) the way shrinkage and creep are modeled in the NLFEA affects the load-bearing capacity of the analyzed element by up to 10%; (3) the displacement capacity is strongly affected by the presence of the transverse diaphragm in the section above the pier, which produces stiffening effects in the critical section and leads to a widened crack pattern spreading over the RC slab. Model uncertainties related to all the concurrent analyzed factors in terms of load-bearing capacity and displacement capacity vary from 5% up to 25%.

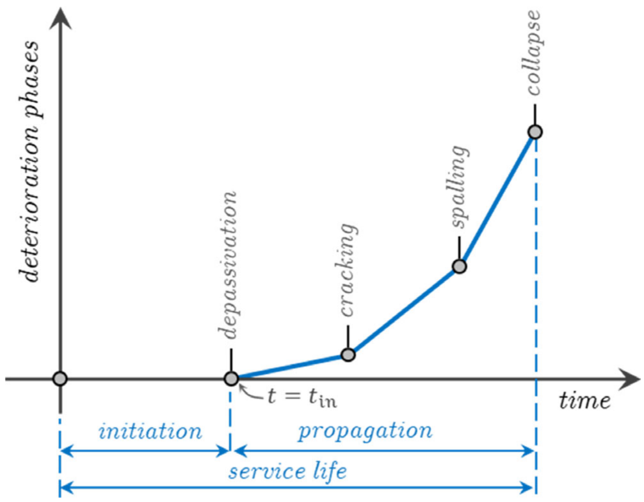

FIGURE 19 Schematic trend of corrosion-induced deterioration process in concrete structures (after Tuutti[53]).

5 | NLFEA INCORPORATING CORROSION MATERIAL DEGRADATION

Chloride and carbonation are the two main sources of corrosion of steel reinforcement.[35] As sketched in Figure 19, corrosion-induced deterioration of concrete structures is typically described by the Tuutti's model,[53] which divides the service life of the structure into two distinct phases[54,55]: the *initiation* (or induction) *period*, in which the concrete *pH* slowly decreases and the aggressive agents (CO_2 or Cl^-) progressively penetrate the concrete shallower layers until approaching the underlying steel bars; and the *propagation period*, in which the steel bars are depassivated, expanding corrosion products are formed and lead to deterioration of surrounding concrete with cracking and subsequent spalling, loss of section until structural collapse. In Figure 19, we have emphasized that the rate of deterioration follows a nonlinear trend over the time, that is, it increases more than linearly with time after depassivation takes place at the initiation time $t = t_{in}$. This can be justified by the fact that cracking, debonding and spalling caused by the rust facilitates the ingress of oxygen, thus accelerating the corrosion process. However, there is no consensus on the quantitative model to describe the overall time propagation of corrosion, with various empirical proposals in the literature.

5.1 | Experimentally calibrated time-dependent corrosion model

The qualitative graph of Figure 19 is taken into account to calibrate a simplified time-dependent corrosion model. The experimental campaign described in Section 3 has highlighted that: (i) no localized pits are present in the steel reinforcement, whereas the oxidation process appears uniformly distributed on the entire surface of steel bars; (ii) the amount of chloride ions obtained by chemical analyses at different depths from 5 to 50 mm is comparable, which suggests that no chloride diffusion process is ongoing, and that the detected chloride content is likely related to an initial contamination of concrete during on-site mixing; (iii) the identified amount of chlorides is below critical contents for typical Portland cements. These observations have led the authors to exclude the presence of pitting corrosion and to justify the hypothesis of carbonation-induced uniform corrosion in the numerical simulation. The road overpasses are indeed located close to CO_2-rich industrial areas (due to the presence of an electrical plant and a petrol-chemical transformation farm in the nearby) with relative humidity between 60% and 90%–95%, depending on seasonal and daily fluctuations, which correspond to high carbonation rates.[56] These factors have likely neutralized the alkalinity of concrete from cover up to the underlying layers (extensive carbonation), as confirmed by the relatively high carbonation depths up to 35 mm that are shown in Figure 5, largely exceeding the concrete cover of 15 mm.

Carbonation depths identified from experimental tests combined with mass losses measured on extracted steel bars are used for calibrating a simplified time-dependent uniform-corrosion model of steel reinforcing bars and prestressing cables, which is embedded in the NLFEA to investigate the influence of corrosion on the load-bearing capacity and failure mechanism of the analyzed Gerber half-joints.

The evolution of carbonation depth is governed by a square-root formulation derived from Fick's diffusion law[57]:

$$x_{CO2}(t) = K\sqrt{t}, \tag{5}$$

where the factor K depends on the ambient carbon-dioxide content at the concrete surface and on the mix design of concrete. Equation (5) is rationally exploited for calculating the factor K a posteriori, based on the average carbonation depth obtained in the experimental campaign $x^*_{CO2} = 23.6\,\text{mm}$ measured at the current time $t^* = 53$ years, which leads to:

$$K = \frac{x^*_{CO2}}{\sqrt{t^*}} = \frac{3.24\,\text{mm}}{\sqrt{\text{years}}}. \tag{6}$$

Once K is known, the initiation time of the corrosion process t_{in} can be obtained by setting $x_{CO2} = c$ in

Equation (5), where $c = 15\,\text{mm}$ represents the concrete cover identified from pachometer tests, which leads to:

$$t_{\text{in}} = \left(\frac{c}{K}\right)^2 = 21.4\,\text{years}. \tag{7}$$

This means that the elapsed propagation time at the current date (53 years from the bridge construction), is equal to $t^*_{\text{prop}} = 31.6\,\text{years}$. The average mass loss at $t = t^* = 53\,\text{years}$ measured in the experimental campaign is $\Delta m(t^*) = \Delta m^* = 4.2\%$ (see Section 3.2), from which one can calculate the average corrosion penetration $P_{\text{corr}}(t = 53\,\text{years}) = P^*_{\text{corr}}$ through Equation (2). As an example, for a 12 mm diameter steel bar we obtain $P^*_{\text{corr}} = 127\,\mu\text{m}$, which corresponds to an equivalent corroded diameter $\phi^* = 11.74$ mm. By dividing the corrosion attack depth P^*_{corr} with the propagation time t^*_{prop} we obtain the average corrosion rate per year during the considered period $\left(t_{\text{in}}, t^*_{\text{prop}}\right)$, V_{corr} in μm/year or, equivalently, the average corrosion current density I_{corr} in $\mu\text{A/cm}^2$ through Faraday's law:

$$V_{\text{corr}}(\mu\text{m/year}) = \frac{P^*_{\text{corr}}}{t^*_{\text{prop}}} = 11.6 \times I_{\text{corr}}\left(\mu\text{A/cm}^2\right). \tag{8}$$

For a 12 mm diameter steel bar $V_{\text{corr}} = 4.03\,\mu\text{m/year}$ and $I_{\text{corr}} = 0.35\,\mu\text{A/cm}^2$ at $t^* = 53\,\text{years}$, which corresponds to a "depassivated condition but in low humidity concrete" according to the RILEM TC 154 recommendations.[58,59] In the graph plotting the corrosion penetration as a function of time $P_{\text{corr}}(t)$ shown in Figure 20, two characteristic points have been found through the interpretation of the experimental results, namely: point A $(t_{\text{in}}, 0)$ identifying the start of depassivation phase; point B $\left(t^*, P^*_{\text{corr}}\right)$ denoting the condition at the current date (31.6 years of elapsed propagation time). Various hypotheses on the trend of the corrosion rate V_{corr} (i.e., the change of slope of P_{corr} vs. time) can be made. In real cases, the instantaneous V_{corr} depends on daily climatic changes, seasonal fluctuations, raining periods, and exposure to the rain, which all affect the concrete degree of saturation. Since cracked concrete reasonably leads to faster diffusion of aggressive agents, various authors have proposed an increase of corrosion rate after concrete cracking, either through a sharp change of slope described by a bilinear propagation model[59] or through a function related to the crack width.[60,61] Other authors have proposed quadratic, exponential, logarithmic, or power-law functions.[62] In this paper, we propose the following quadratic law:

$$P_{\text{corr}}(t) = \begin{cases} 0 & , \text{for } 0 \le t \le t_{\text{in}} \\ P^*_{\text{corr}} \cdot \left(\dfrac{t - t_{\text{in}}}{t^*_{\text{prop}}}\right)^2 & , \text{for } t > t_{\text{in}} \end{cases} \tag{9}$$

that is plotted in Figure 20 and compared to other empirical formulations. This model is useful to extrapolate the corrosion attack depth for $t > t^*$: in particular, the predictions of the proposed quadratic model after 60 years of service life are quite close to those of a so-called multilinear corrosion propagation model, which is obtained by increasing the instantaneous corrosion rate V_{corr} of a factors 2, 3, and 4 after time intervals equal to t_{in}, that is, V_{corr} is doubled from $2t_{\text{in}}$ to $3t_{\text{in}}$, is tripled from $3t_{\text{in}}$ to

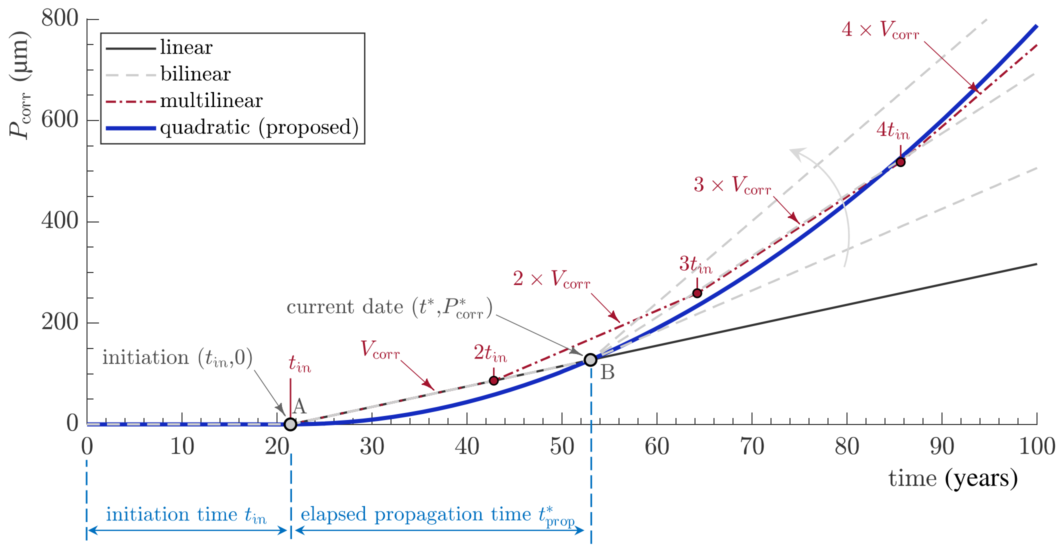

FIGURE 20 Comparison among various corrosion propagation models fitted to experimental results of the *in situ* test campaign.

TABLE 5 Equivalent diameter and cross-sectional area of corroded steel bars in two phases of the service life.

Uncorroded scenario		Corrosion scenario at $t = 53$ years		Corrosion scenario at $t = 100$ years	
Diameter	Area	Equivalent diameter	Equivalent area	Equivalent diameter	Equivalent area
ϕ_0 (mm)	A_0 (mm^2)	ϕ^* (mm)	A^* (mm^2)	ϕ^* (mm)	A^* (mm^2)
7	38.48	6.74	35.68	5.39	22.83
8	50.27	7.74	47.05	6.39	32.08
10	78.54	9.74	74.51	8.39	55.30
12	113.10	11.74	108.25	10.39	84.81
14	153.94	13.74	148.27	12.39	120.60
24	452.39	23.74	442.64	22.39	393.78

$4t_{in}$ and so forth. This hypothesis reflects the progressive increase of corrosion rate ascribed to concrete microcracking, cracking and spalling over the structural service life, as qualitatively sketched in the previous Figure 19.

Once the variation of corrosion penetration with time $P_{corr}(t)$ is calculated, Equation (3) can be used to estimate the residual bar diameter at any phase of the structural service life. We focus the attention on two conditions, namely the current date $t = 53$ years and the typical design service life of bridge structures $t = 100$ years.[63] Corresponding residual diameters for the steel bar diameters involved in the analyzed road overpasses are listed in Table 5.

A corrosion scenario for the prestressing cables, formed by a group of N straight Ø7 steel wires, is also considered. The main cause of corrosion of the prestressing cables is the ingress of aggressive agents inside the duct due to an imperfect grouting or a defective sealing at the anchor heads. In real cases, we expect that the corrosion attack has a predominant direction or a less severity than a single bar; consequently, to develop a preliminary, simplified model, it can be assumed that for a cable composed of N wires only a fraction k of the internal wires (with $k < N$) is more exposed to the corrosive agents and is affected by the corrosion-induced degradation, whereas the remaining $N - k$ wires can be considered uncorroded, see Figure 21. For the k corroded Ø7 steel wires we use the same approach (corrosion rate) as for the ordinary steel bars: equivalent corroded diameter and corroded area for the single Ø7 steel wire are listed in the first row of Table 5. Denoting with $A_{0,Ø7}$ the area of the uncorroded wire and with $A^*_{Ø7}$ the corresponding corroded area, the area of the corroded prestressing cable is calculated as follows:

$$A^*_{cable} = A^*_{Ø7} \times k + A_{0,Ø7} \times (N - k). \tag{10}$$

To the best of the authors' knowledge, there is no universal consensus on a reliable corrosion diffusion model for grouted posttensioned prestressing cables. While the corrosion scenario is strongly affected by the environmental factors and exposure conditions, which change from case to case, it is reasonable to postulate a lower severity of corrosion attack compared to that affecting the surrounding ordinary steel bars because the prestressing posttensioned cables are generally placed within metallic ducts at a slightly higher distance from the concrete external surface (although in the present case the cables 3 and 4 even cross the overlying RC slab and are very close to the external surface; see again Figure 3). These considerations justify the value $k < N$; however, the specific selection of the weight factor k, calibrated upon the boundary conditions, certainly deserves further investigation by means of laboratory specimens under controlled corrosion scenarios in future studies. In this paper, a hypothetical corrosion scenario $k = N/3$ is considered to explore the impact of a simultaneous corrosion of both skin reinforcement and prestressing cables by accounting for a different extent of the deterioration phenomenon. Values of the equivalent corroded area of the prestressing cable obtained by assuming a fraction $k = N/3$ in the considered corrosion scenarios are listed in Table 6: based on the proposed approach, the overall mass loss of the prestressing cable is equal to 2.43% at 53 years, and 13.56% at 100 years.

5.2 | Influence of corrosion on the load-bearing capacity and failure mechanism

Among the four models presented in Section 4, for the sake of brevity, the influence of corrosion is analyzed by focusing the attention on models M2 and M4 only because: (1) the results of model M2 can be straightforwardly compared to those obtained by simplified formulations used in engineering practice, like STM and cross-sectional flexural analyses, which typically adopt an "implicit" formulation (in the meaning used in

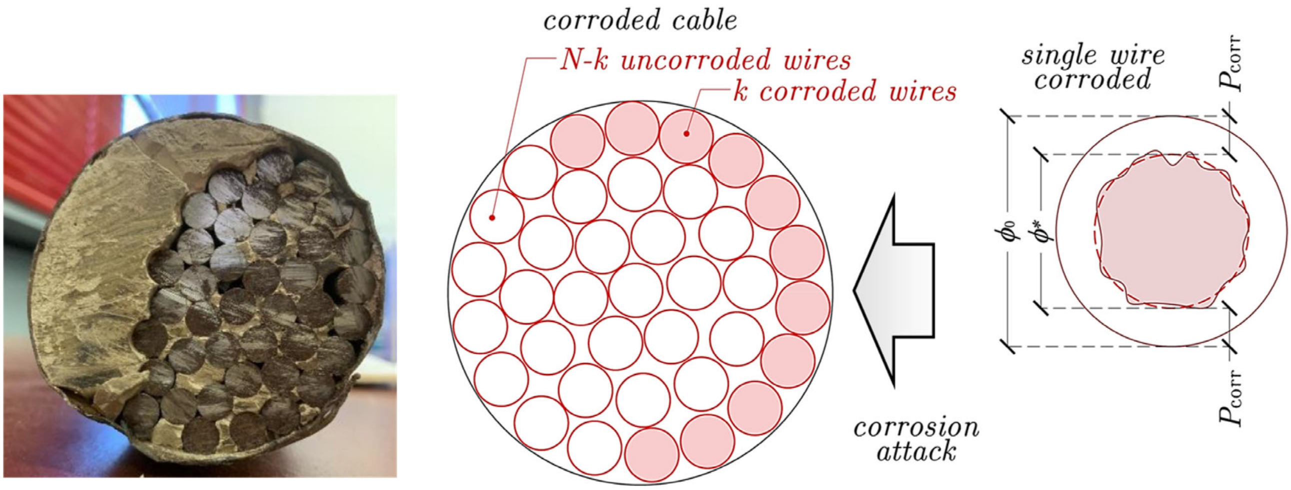

FIGURE 21 Cross section of an uncorroded prestressing cable with Ø7 straight wires (left) and hypothesis of cable corrosion (right).

TABLE 6 Equivalent cross-sectional area of prestressing cables in two phases of the service life obtained with $k = N/3$ in Equation (10).

Uncorroded scenario		Corrosion scenario at t = 53 years	Corrosion scenario at t = 100 years
Prestressing cable	Area $A_{0,\text{cable}}$ (mm^2)	Area A^*_{cable} (mm^2)	Area A^*_{cable} (mm^2)
32 wires	1231.50	1201.58	1064.52
42 wires	1616.35	1577.07	1397.18

this paper) to account for shrinkage and creep deformations of concrete, as discussed in the following section; (2) the results from 2D and 3D NLFEAs for models M2 and M4 in the uncorroded scenario are very close to each other (see Figure 14), which makes it possible to focus on the effects of corrosion in a more targeted way reducing other model uncertainties. It is worth remarking that the larger displacement capacity attained by model M4 should be conservatively verified in relationship to the entire deck model, not just a portion of the model, which is beyond the scope of the present paper and is left for future research work.

Load–displacement curves obtained for the corroded models by 2D and 3D NLFEAs are shown in Figure 22, while the corresponding values of peak load $P_{\max}$ and displacement capacity $d_{\max}$ are listed in Table 7. Corrosion-related deterioration has led to a negligible reduction of the load-bearing capacity (<2% in both 2D and 3D NLFEAs) at the current date (53 years from the construction), whereas it has produced a moderate decrease of the peak load (variable from 7% to 10%) at 100 years of service life. The displacement capacity is slightly increased in passing from the uncorroded to the corroded scenarios, especially in the 3D NLFEAs: this is reasonable as the steel strain of the reduced-area reinforcement bars and cables in the tensile zone must increase to satisfy the equilibrium with the external actions; therefore, a larger portion of the plastic branch of the steel constitutive relationship is exploited in the corroded scenarios. A similar behavior was also noted in previous studies on the seismic vulnerability of corroded bridge piers.[7] Overall, the results from 2D and 3D NLFEAs are in reasonable agreement with each other.

As to the failure mechanism, it is noted in Figure 23 that the effect of the reduced cross-sectional area of the steel reinforcement has led to a wider damage zone in the tensile region of the RC slab compared to the uncorroded case. Similarly to the uncorroded case, the ultimate behavior is dominated by the negative bending moment in the section above the pier support, while the shear in the re-entrant corner does not constitute the governing mechanism even under a realistic corrosive scenario. Localized crushing of compressed concrete is also observed near the pier support region.

6 | COMPARISON WITH SIMPLIFIED FORMULATIONS

Although the results from 2D and 3D NLFEAs appear consistent and in reasonable agreement with each other,

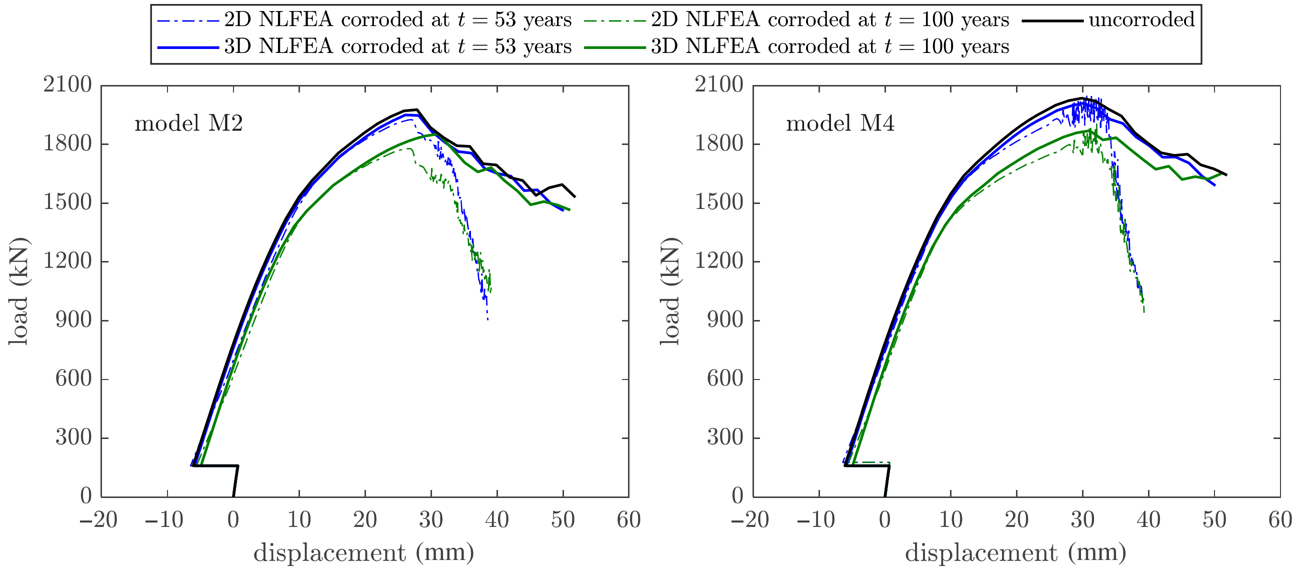

FIGURE 22 Load–displacement curves obtained by 2D and 3D nonlinear finite element analysis (NLFEAs) on corroded models of the Gerber half-joint.

TABLE 7 Results of nonlinear finite element analysis in terms of peak load P_{max} and displacement attained at peak load d_{max} (displacement capacity) for corroded Gerber half-joint in two phases of the service life.

	2D model (VecTor2[42])		**3D model (ATENA[48])**	
Model ID	P_{max} **(kN)**	d_{max} (mm)	P_{max} **(kN)**	d_{max} (mm)
M2 corroded at $t = 53$ years	1926	26.4	1949	26.1
M2 corroded at $t = 100$ years	1778	26.1	1853	31.1
M4 corroded at $t = 53$ years	2049	30.0	2010	30.1
M4 corroded at $t = 100$ years	1905	31.5	1870	31.1

the validity of the FE predictions remains unproven since the analyzed road overpasses are in service conditions and cannot be tested. Indeed, the validity of the FE predictions is the main drawback of the study, as there is no experimental validation, which represents a limitation of the study. To critically assess the order of magnitude of the peak loads obtained from NLFEAs, the load-bearing capacity of the analyzed Gerber half-joints is also estimated through simplified approaches based on models and hypotheses commonly used in engineering practice. The analyzed portion of the road overpasses involves three resisting mechanisms that are studied independently via three corresponding simplified models: (1) resisting shear mechanism in the half-joint (D-region) investigated through the STM proposed by the EC2-1[52]; (2) resisting flexural mechanism activated by negative bending moment in the section above the pier investigated through basic cross-sectional analysis (*flexural capacity*); and (3) resisting shear mechanism in the section close to the pier, investigated through the simplified modified compression field theory (*SMCFT*) formulation[64] as implemented in the recent Model Code 2020 (MC2020).[65]

6.1 | Shear capacity in the half-joint through STM

With regard to the STM, the EC2-1[52] proposes two qualitative schemes named A and B in Figure 24, which are here considered additive and adapted to the geometry and reinforcement arrangement of the case study. Struts are depicted with dashed blue lines and denoted with "C" labels, whereas ties are marked with continuous red lines and denoted with "T" labels. Model A relies on vertical stirrups (tie T_2) and horizontal reinforcement (T_1 and T_3), whereas model B accounts for diagonal bars (tie T'_1). The ultimate capacity of each strut-and-tie is given by:

$$C_i = b_i t_i f^*_{cm}; \qquad T_i = A_{si} f_{ym}, \tag{11}$$

where b_i and t_i represent the width and thickness of the ith strut, respectively, $f^*_{cm} = \nu f_{cm}$ is the reduced concrete strength, ν being an efficiency factor for concrete cracked in shear, A_{si} is the cross-sectional area of the ith reinforcement and f_{ym} the corresponding yield strength.

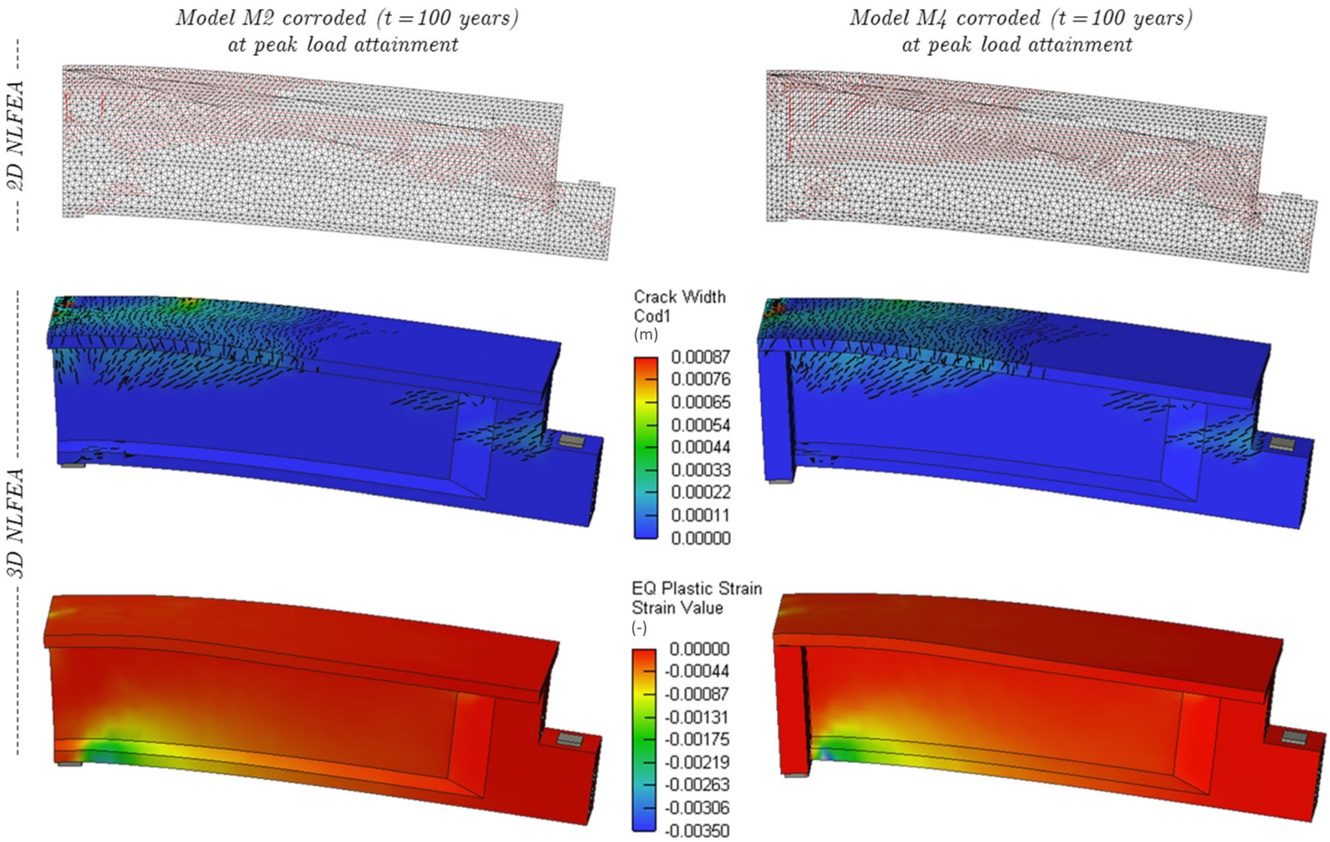

FIGURE 23 Failure mechanisms obtained by 2D and 3D nonlinear finite element analysis (NLFEAs) on corroded M2 and M4 models.

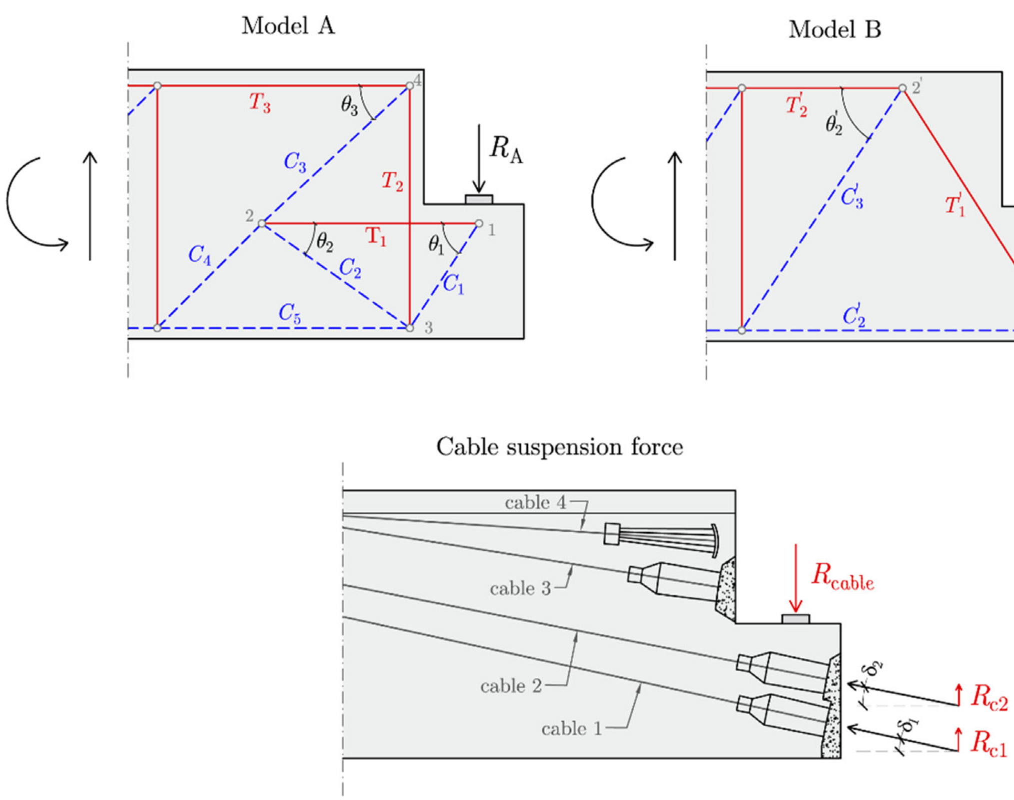

FIGURE 24 Strut-and-tie models based on EC2-1[52] adapted to the geometry and reinforcement arrangement of the case study (top) and suspension contribution of the cable force (bottom).

Detailed expressions of all strut-and-tie capacities, based on equilibrium conditions of the nodes, can be found in a previous paper.[14] Cable 4 is incorporated in the horizontal ties T_3 and T'_2, whereas the vertical prestress component of cables 1 and 2 anchored in the protruding nib of the half-joint is taken into account explicitly in the calculation of the shear capacity as follows:

$$R^{\mathrm{STM}} = R_{\mathrm{A}} + R_{\mathrm{B}} + R_{\mathrm{cable}}, \tag{12}$$

where R^{STM} denotes the overall shear resistance of the STM, R_{A} and R_{B} are the contributions of the two models A and B separately. In Equation (12), R_{cable} is the vertical component of the cable force (suspension contribution) given by:

$$R_{\mathrm{cable}} = \left(A_{\mathrm{cable1}} \times \sin\left(\delta_{\mathrm{p1}}\right) + A_{\mathrm{cable2}} \times \sin\left(\delta_{\mathrm{p2}}\right)\right) \times \sigma_{\mathrm{p\infty}} \tag{13}$$

where $A_{\mathrm{cable}i}$ is the cross-sectional area of the ith cable, δ_i is the corresponding inclination angle with respect to the horizontal axis (see again Figure 24), and $\sigma_{\mathrm{p\infty}} = \sigma_{\mathrm{p0}} - \Delta_{\sigma_{\mathrm{p}}}$ is the prestress in the cable after all losses calculated according to EC2-1 expressions.[52] For the cable suspension force we assume a stress level $\sigma_{\mathrm{p\infty}}$ (rather than $f_{\mathrm{p(0.1)}}$ or f_{pu}) because it is reasonably expected that the prestressing cables do not experience any significant stress increase at failure given that such section is close to the half-joint and is ideally undergoing zero bending moment.

Some struts or ties are overlapped in the schemes A and B, which implies that their resistance should be properly split in the two additive models to maximize the shear capacity in accordance with the lower-bound theorem of plasticity.[66–68] This is done by introducing a weight factor ξ of the overlapping struts or ties as free design parameter, for example, ξT_3 and $(1-\xi)T'_2$, or ξC_5 and $(1-\xi)C'_2$. Moreover, in the model A the tie T_2 involves vertical hangers 2Ø24 plus some stirrups Ø14 whose number n_{st} represents another free design parameter that can be varied to maximize the shear capacity in Equation (12), as the extent of the tensile region in the failure mechanism is not known a priori, see Figure 25. Consequently, the evaluation of R^{STM} in Equation (12) entails a nonlinear constrained multivariable optimization problem of the shear capacity by varying ξ and n_{st} within a reasonable interval [0–1] and [0–8], respectively. At the end of the optimization process, the number of stirrups is obviously rounded to the integer closest to the optimal detected solution. As an example, in Figure 26 the optimal solution $R^{\mathrm{STM}} = 1780\,\mathrm{kN}$ for the uncorroded Gerber half-joint is associated with design parameters $\xi \approx 0.5$ and $n_{\mathrm{st}} = 4$.

It is worth noting that the STM configuration of model A sketched in Figure 24 and reported in the EC2-1[52] has been criticized by some authors,[69] because the tie T_1 would be anchored by the strut C_2 in a zone that typically exhibits cracking due to tensile forces. An alternative STM configuration was proposed by Schlaich et al.[70,71] that avoids this problem, as illustrated in Figure 27. Using this alternative model A in place of that suggested by the EC2-1 in Figure 24 and combining it with model B has led to higher values of the shear capacity, as will be discussed in Section 6.4. Moreover, according to Schlaich and Schäfer,[71] the superposition of the two models (A and B) is realistic provided the combined models satisfy specific requirements on the angles θ_i between struts and ties: for struts and ties with relatively high forces, these angles should be chosen larger than 45° to avoid incompatibility problems. However, these

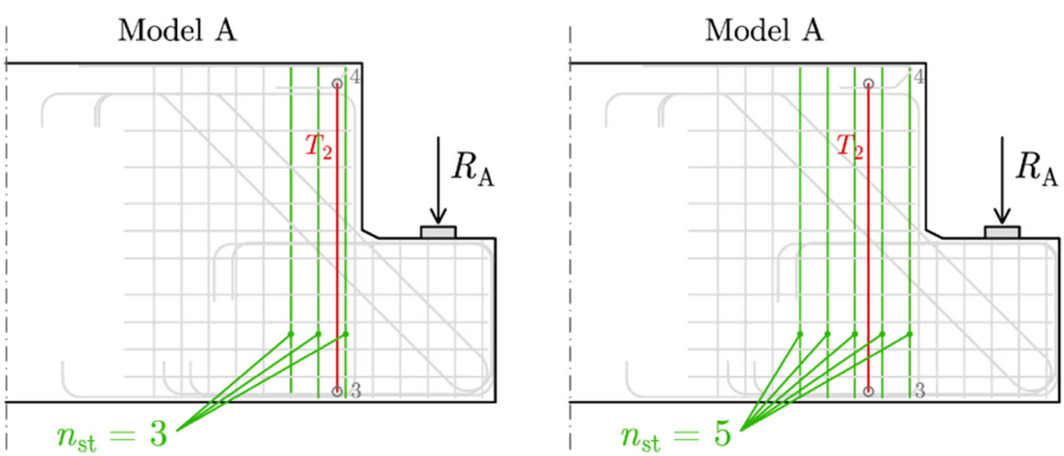

FIGURE 25 Meaning of the free design parameter n_{st} in the optimization (maximization) of the shear capacity R^{STM}.

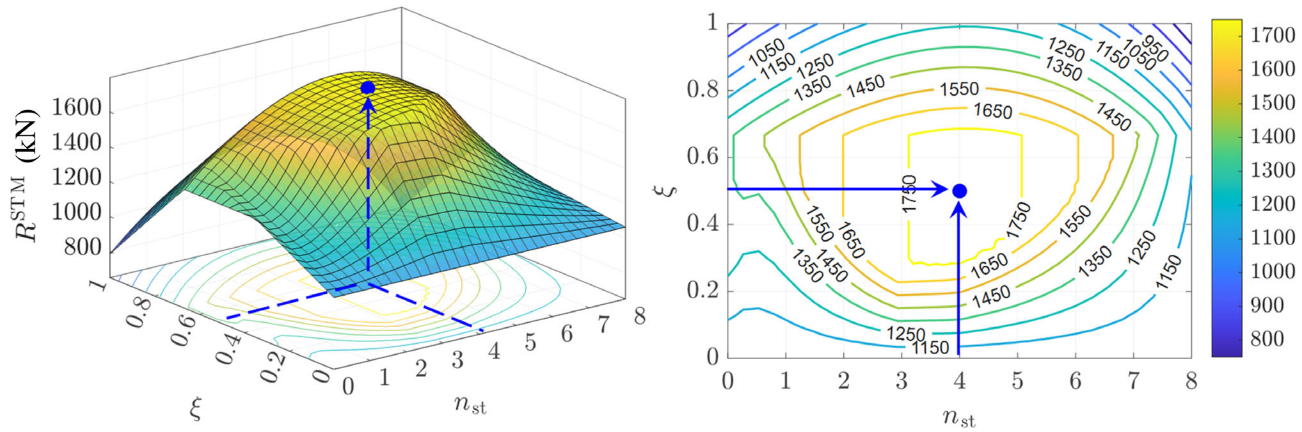

FIGURE 26 Nonlinear constrained multivariable optimization problem for determining R^{STM} in Equation (12): Surface plot (left) and contour plot (right) in the search space.

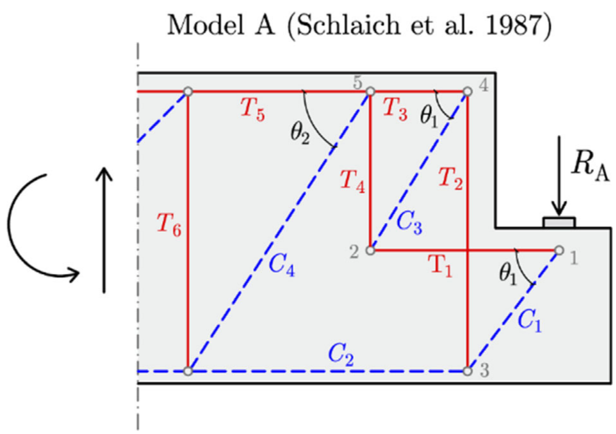

FIGURE 27 Alternative strut-and-tie models configuration (model A) proposed by Schlaich et al.[70,71]

requirements are hardly satisfied in the case of model A of the EC2-1[52] (see, e.g., the angle θ_2 forming between C_2 and T_1 in Figure 24), whereas they can be more easily satisfied in the alternative model A proposed by Schlaich et al.[70,71]

6.2 | Flexural capacity in the section above the pier through sectional analysis

With regard to the flexural capacity in the section above the pier subject to negative bending moment, we use traditional hypotheses for determining the ultimate bending resistance,[72] namely: (1) plane sections remain plane; (2) perfect bond at the concrete-steel interface (although, in general terms and for other structures different from those analyzed in this work, this represents a simplifying hypothesis in a deteriorated component that exhibits carbonation-induced uniform corrosion); (3) tensile strength of concrete is ignored; (4) compressive stresses in the concrete are derived from a rectangular stress-block constitutive model; (5) stresses in the prestressing steel cables are derived from an elasto-plastic model with strain hardening; (6) ultimate compressive strain in the concrete is assumed equal to 0.0035; (7) stresses in the ordinary steel bars are neglected for simplicity. Moreover, the initial strain in the prestressing tendons is taken into account when determining the stresses in the tendons. Such initial strain is considered after all stress losses (including shrinkage- and creep-related phenomena), this is why it is more appropriate to compare the results of the simplified analyses with NLFEA results obtained in model M2.

6.3 | Shear capacity in the section close to the pier through SMCFT

Finally, the shear capacity of the section close to the pier (strictly speaking, an effective depth d far from the pier section) is calculated through the recent MC2020 formulation[65]: we use the level of approximation (LoA) IIb that is inspired to the SMCFT[64] and establishes a fixed value for the strut inclination angle θ based on the longitudinal strain at the mid-depth of the effective shear depth ε_x, meant as the "representative" strain,[73] see Figure 28. The shear capacity V_{Rd} in LoA IIb is given by the sum of the concrete contribution $V_{\mathrm{Rd,c}}$ and of the shear contribution $V_{\mathrm{Rd,s}}$:

$$V_{\mathrm{Rd}} = V_{\mathrm{Rd,c}} + V_{\mathrm{Rd,s}} \leq V_{\mathrm{Rd,max}}, \tag{14}$$

in which

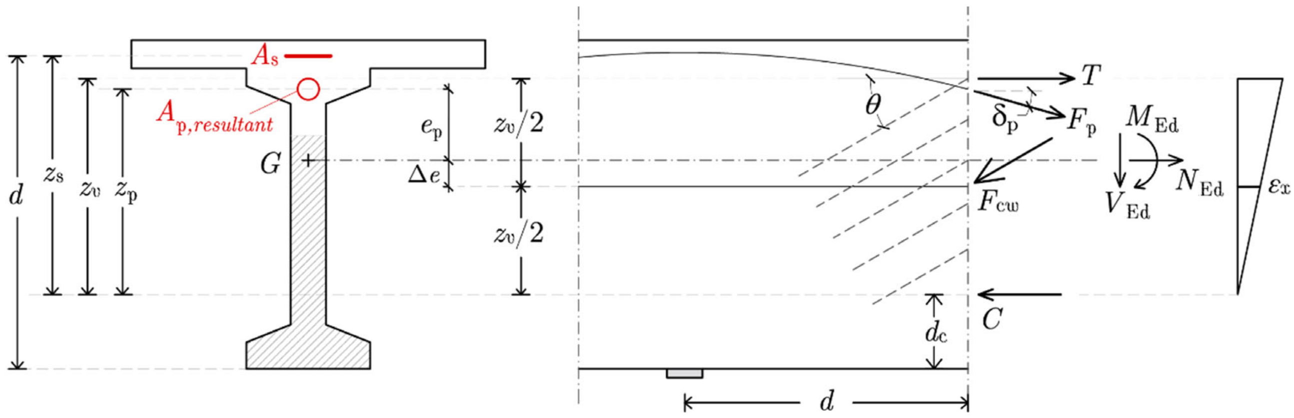

FIGURE 28 Scheme for the shear strength calculation in the pier section (intermediate support region) according to MC2020.[65]

$$V_{\mathrm{Rd,c}} = \frac{k_{\mathrm{v}}\sqrt{f_{\mathrm{ck}}}}{\gamma_{\mathrm{c}}} b_{\mathrm{w}} z_{\mathrm{v}}; \quad V_{\mathrm{Rd,s}} = \frac{A_{\mathrm{sw}}}{s_{\mathrm{w}}} z_{\mathrm{v}} f_{\mathrm{ywd}} \cot\theta; \quad V_{\mathrm{Rd,max}} = \frac{k_{\varepsilon} f_{\mathrm{cd}} b_{\mathrm{w}} z_{\mathrm{v}}}{\cot\theta + \tan\theta}, \tag{15}$$

where $k_{\mathrm{v}} = f(\varepsilon_{\mathrm{x}})$ is a reduction coefficient of the tensile strength of concrete, function of the mid-depth strain ε_{x}; γ_{c} is the partial safety factor of concrete (assumed unitary for verification purposes); b_{w} is the web width; z_{v} is the effective shear depth that would be $0.9d$ in RC members (d being the effective flexural depth), but in prestressed members is taken as the distance from the resultant of the compressive chord force C to the resultant of tensile forces T and F_{p} pertinent to ordinary steel reinforcement (having cross-sectional area A_{s}) and prestressing tendon (having cross-sectional area A_{p}), respectively, and can be determined by assuming proportionality conditions and elastic behavior with equal moduli of elasticity for both types of steel,[73] which yields $z_{\mathrm{v}} = \left(z_{\mathrm{s}}^2 A_{\mathrm{s}} + z_{\mathrm{p}}^2 A_{\mathrm{p}}\right)/\left(z_{\mathrm{s}} A_{\mathrm{s}} + z_{\mathrm{p}} A_{\mathrm{p}}\right)$, z_{s} and z_{p} being the distances between the compressive chord and the reinforcement and tendon axes, respectively; A_{sw} is the cross-sectional area of shear reinforcement and s_{w} the spacing of stirrups; f_{ywd} is the yield strength of shear reinforcement; $\theta = f(\varepsilon_{\mathrm{x}})$ is the compressive stress field inclination, function of the mid-depth strain ε_{x}; k_{ε} is a strength reduction factor of concrete carrying the compression field that depends on ε_{x} and θ. By conservatively assuming a triangular strain distribution with zero value at the compression chord as shown in Figure 28 (right), the mid-depth strain ε_{x} can be calculated as half of the tension chord strain, that is, $\varepsilon_{\mathrm{x}} = T/2EA$, where the tensile force T depends on the external actions, namely normal force N_{Ed}, bending moment M_{Ed}, and shear force V_{Ed}, including the effects of the inclined tendon force F_{p}. However, at ultimate conditions $V_{\mathrm{Ed}} = V_{\mathrm{Rd}}$ is unknown, consequently V_{Rd} depends on ε_{x} and vice versa, which requires an iterative procedure. Within such iterative procedure, the bending moment M_{Ed} is assumed to increase linearly with the shear force $V_{\mathrm{Ed}} = V_{\mathrm{Rd}}$ through a fixed shear factor a calculated from the design values as $a = M_{\mathrm{Ed},0}/V_{\mathrm{Ed},0}$.

6.4 | Comparison of the load-bearing capacity and critical discussion

The load-bearing capacity of the Gerber half-joint is evaluated through such simplified approaches, considering the three resisting mechanisms individually, and is compared to the NLFEA results of model M2 in Figure 29. As expected, the simplified methods generally produce more conservative estimates of the load-bearing capacity than NLFEAs (around 10% lower), in line with other literature studies.[13] It is noted that the STM configuration with model A proposed by Schlaich et al.[70] is associated with higher load-bearing capacity (more than 15% for the uncorroded case and corroded case at 53 years, and slightly more than 10% for the corroded case at 100 years) than that associated with the STM proposed by the EC2-1.[52] Such comparison between the two alternative strut-and-tie configurations demonstrates that the selection of the most appropriate statically and plastically admissible solution is crucial in the evaluation of the ultimate capacity in the STM. Values of the ultimate load of the three analyzed simplified mechanisms also give some hints on the expected failure mode, which is related to the weakest mechanism, that is, the one corresponding to the lowest load-bearing capacity among those considered in the simplified methods. The results indicate that the flexural failure is the weakest, dominant mechanism of the analyzed Gerber half-joint in the uncorroded scenario (1693 kN) and in the corroded case at 53 years (1682 kN). This is related to the peculiarity of the analyzed elements that present an inadequate concrete compressed area in the section above the pier subject to negative bending moment; consequently, the inner lever arm at ultimate conditions is relatively low, with a

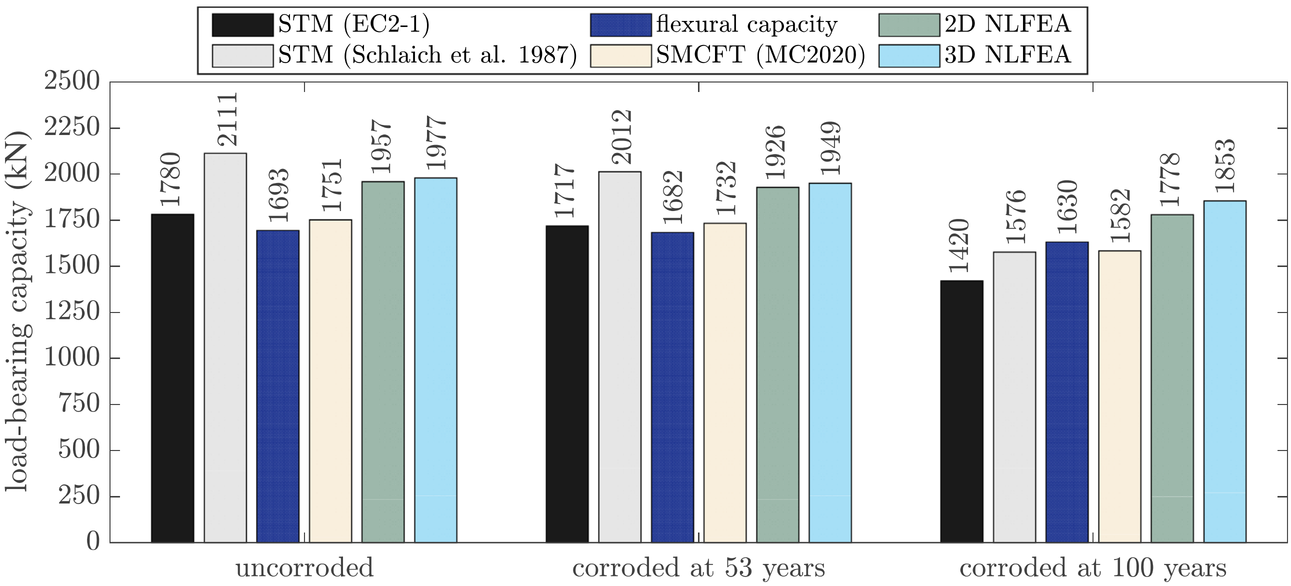

FIGURE 29 Load-bearing capacity of Gerber half-joint evaluated through different models in the uncorroded and corroded scenarios. NLFEA, nonlinear finite element analysis; SMCFT, simplified modified compression field theory; STM, strut-and-tie models.

neutral axis depth roughly equal to 110 cm in both uncorroded and corroded (at 53 years) scenarios, thus cutting more than two-thirds of the girder web height as qualitatively shown in Figure 28. Moreover, these results confirm that shear-related failures in the half-joints, which can represent the most vulnerable mechanism in this kind of RC half-joint overpasses,[19] do not constitute the governing failure mode in the present case study and this is ascribed to the large quantity of hangers and diagonal steel bars in the half-joint. However, more severe reductions of the cross-sectional area of the steel reinforcement in the corroded scenario at 100 years generate a proportional decrease of the shear capacity in the dapped end calculated by the STM (1576 kN for the model proposed by Schlaich et al.[70]), thus suggesting that the collapse mechanism could apparently change from a flexural failure in the section above the pier to a shear failure in the half-joint.

In a hypothetical more efficient design of similar bridges, a wider bottom flange in the girder cross section should be present so that the inner lever arm increases, and the flexural capacity would get higher accordingly. While this might appear as a design drawback of the analyzed structures, we emphasize that such apparently inefficient shape of the girder cross section represents a peculiarity of all the PC highway overpasses located in Sicily, southern Italy, distributed along the A20 highway (Messina-to-Palermo) and A18 highway (Messina-to-Catania). Two of these overpasses of the A20 highway were also closed to traffic and demolished for safety reasons some years ago. This is why, in the authors' opinion, this contribution represents an interesting and emblematic case study covering a large part of the infrastructure network of the Sicilian region and involving several bridge structures with high traffic frequency. The results of this numerical study, if properly complemented by further experimental (full-scale) measurements on the analyzed overpasses, could be used by the bridge management companies to carry out large-scale safety assessments and to implement timely and precise structural interventions in specific, critical zones of such infrastructure network.

Overall, the results from the simplified approaches are quite consistent with those obtained by the NLFEAs. From a practical design and assessment perspective, these results can be viewed as an interesting comparison among alternative levels of approximation associated with different levels of accuracy[65]: the simplified approaches, like STM and cross-sectional analyses, represent the simplest and most straightforward methods belonging to an hypothetical LoA I, while 2D and 3D NFLEAs, capable of simulating the correct geometry and reinforcement layout of the element and the progressive development of deformations taking into account the effects of applied loads, prestressing, nonlinear behavior of concrete and steel, are associated with higher levels of accuracy, require more computational effort but reasonably lead to more economic solutions.

The ultimate capacity obtained in this paper by NLFEAs is restricted to a single portion of the bridge deck, namely one longitudinal beam. Strictly speaking, the flexural failure of the mostly loaded beam section over the pier will not produce the failure of the entire bridge deck because stress redistribution between adjacent girders could take place due to the presence of transverse diaphragms. In previous studies dealing with the ultimate capacity of similar grillage deck schemes under a flexure-dominated failure,[5,74] such redistribution effects led to values of the ultimate capacity of the entire bridge deck around 10%–15% higher than the ultimate capacity of the single mostly loaded girder. In this regard, the values of peak load obtained in this study should be meant as conservative estimates of the load-bearing capacity of the overall bridge deck because the redistribution effects were neglected. Based on the sectional features of the longitudinal girders and the observed neutral axis depth in the section over the pier, it is expected that the rotational ductility and, consequently, the internal stress redistribution of the present case study will be relatively modest. The extension of the NLFEAs by explicitly modeling all longitudinal girders and transverse diaphragms constituting the entire bridge deck to quantify such redistribution effects certainly deserves further investigation and represents the object of ongoing research whose results will be presented in forthcoming papers.

7 | CONCLUSIONS AND FUTURE DEVELOPMENTS

This paper has investigated the structural behavior of a peculiar set of deteriorated Gerber half-joints by means of parametric 2D and 3D NLFEAs as well as simplified approaches. The analyzed elements, belonging to a series of road overpasses in the A20 highway in the province of Messina, Italy, present a state of uniform carbonation-induced corrosion of the steel reinforcement. Carbonation depths identified from an extensive *in situ* experimental campaign combined with actual mass losses measured on steel bars extracted from the road overpasses have been rationally used to calibrate a simplified uniform-corrosion model. This model has been incorporated into the NLFEAs to investigate the influence of corrosion on the load-bearing capacity and failure mechanism of the investigated Gerber half-joints.

Parametric NLFEAs on the uncorroded elements critically combined with results from simplified approaches have revealed that:

- the collapse mechanism is dominated by flexural failure in the section above the pier, with a diffuse cracking in the top RC slab starting from the section above the pier subject to negative bending moment and spreading laterally, accompanied by concrete crushing localized in the bottom part of the girder cross section near the support. This is related to the peculiarity of the analyzed elements that present an inadequate concrete compressed area in the section above the pier subject to negative bending moment. The inner lever arm at ultimate conditions in a simplified cross-sectional analysis is indeed relatively low. On the contrary, the shear in the re-entrant corner does not constitute the governing mechanism due to the large quantity of hangers and diagonal steel bars in the half-joint;
- the way concrete shrinkage and creep deformations are modeled in the NLFEA affects the load-bearing capacity of the analyzed element. The so-called implicit formulation, an approach typically used in engineering practice for design and verification of PC members that consists of applying stress losses to prestressing cables based on shrinkage and creep deformations in surrounding concrete, has led to values of peak load around 10% higher than the explicit formulation, the latter meant as the application of isotropic contraction to all concrete finite elements;
- when a portion of the transverse diaphragm in the section above the pier is included in the NLFEA, the displacement capacity increases up to 25% compared to the models without transverse diaphragm and the critical section moves slightly toward the half-joint.

NLFEAs have been performed in two corrosion scenarios, namely at the current date (53 years from the construction) and at 100 years of service life, by simulating the corresponding mass losses of corroded steel bars and prestressing cables through an experimentally calibrated corrosion propagation model. These analyses have revealed that:

- the investigated corrosion scenario leads to a negligible reduction of the load-bearing capacity (<2% in both 2D and 3D NLFEAs) at the current date, whereas it produces a moderate decrease of the peak load (variable from 7% to 10%) at 100 years of service life;
- a wider damage zone arises in the tensile region of the RC slab compared to the uncorroded case. Despite minor variations with respect to the uncorroded case, the flexural failure in the section above the pier support subject to negative bending moment still constitutes the governing mechanism even under a realistic corrosive scenario;
- estimates of the load-bearing capacity provided by simplified approaches are around 10% lower than those obtained by NLFEAs in both uncorroded and corroded cases. This is in line with the philosophy of the levels of approximation suggested by modern design codes, in which the inherent conservatism of the lower levels

is contrasted by more economical solutions of refined, but also more computationally expensive, NLFEAs.

The conclusions drawn here are based on the numerical findings and the comparison with simplified formulations. Without any experimental validation, it is not known if the NLFEA reflects the correct behavior of the full-scale structure. However, the numerical approach presented here can be useful to simulate the impact of corrosion on the ultimate behavior of concrete half-joint bridges different from those considered in this paper. As further developments of this study, we aim to extend NLFEAs to the entire bridge deck, by more appropriately modeling the actual effects of the transverse diaphragm in the vertical load distribution. Although the dominant flexural failure mode obtained in the nonlinear analyses is mainly due to the above-mentioned peculiar shape of the girder cross-section, slightly different failure modes might be observed with alternative load configurations associated with different moment-to-shear ratios, which could be analyzed in future work. Some corrosion-induced degradation effects like reduction of ductility have been purposely ignored in this analysis but might be relevant to situations involving severe pitting corrosion. Moreover, the large quantity of ordinary reinforcement in the half-joint and the observed anchorage lengths of the steel bars have induced the authors to exclude anchorage failure a priori, although this assumption might be a limitation for other conditions or case studies.[75]

ACKNOWLEDGMENTS

The study presented was carried out as part of the program of activities involved in the agreement between the ReLUIS Interuniversity Consortium and the Superior Council of Public Works stipulated pursuant to art. 3 of the Decree of the Minister of Infrastructure no. 578 of 17 December 2020; however, this publication does not necessarily reflect the Council's position and assessments.

DATA AVAILABILITY STATEMENT

The data that support the findings of this study are available from the corresponding author upon reasonable request.

ORCID

Dario De Domenico https://orcid.org/0000-0003-1279-9529
Nino Spinella https://orcid.org/0000-0002-2594-2016
Davide Messina https://orcid.org/0000-0003-2502-8520
Matteo Mazzeo https://orcid.org/0009-0000-6088-0984
Antonino Recupero https://orcid.org/0000-0002-9209-0925

REFERENCES

1. Cosenza E, Losanno D. Assessment of existing reinforced-concrete bridges under road-traffic loads according to the new Italian guidelines. Struct Concr. 2021;22:2868–81. https://doi.org/10.1002/suco.202100147
2. Pinto PE, Franchin P. Issues in the upgrade of Italian highway structures. J Earthq Eng. 2010;14:1221–52. https://doi.org/10.1080/13632461003649970
3. Bazzucchi F, Restuccia L, Ferro GA. Considerations over the Italian road bridge infrastructure safety after the Polcevera viaduct collapse: past errors and future perspectives. Frat Integrita Strutt. 2018;46:400–21. https://doi.org/10.3221/IGF-ESIS.46.37
4. Nuti C, Briseghella B, Chen A, Lavorato D, Iori T, Vanzi I. Relevant outcomes from the history of Polcevera viaduct in Genova, from design to nowadays failure. J Civ Struct Heal Monit. 2020;10:87–107. https://doi.org/10.1007/s13349-019-00371-6
5. De Domenico D, Messina D, Recupero A. Quality control and safety assessment of prestressed concrete bridge decks through combined field tests and numerical simulation. Structure. 2022;39:1135–57. https://doi.org/10.1016/j.istruc.2022.03.086
6. Gandelli E, Rossini G, Mantelli SG, Minelli F. Damage detection of prestressed concrete beams affected by shear and flexure cracks through vibration monitoring. Eng Struct. 2024;304:117572. https://doi.org/10.1016/j.engstruct.2024.117572
7. De Domenico D, Messina D, Recupero A. Seismic vulnerability assessment of reinforced concrete bridge piers with corroded bars. Struct Concr. 2023;24:56–83. https://doi.org/10.1002/suco.202200378
8. Palmisano F, Asso R, Chiaia B, Marano GC, Pellegrino C. Structural assessment of existing R.C. Half-joint bridges according to the new Italian guidelines. J Civ Struct Heal Monit. 2023;13:1551–75. https://doi.org/10.1007/s13349-022-00652-7
9. Rosso MM, Asso R, Aloisio A, Di Benedetto M, Cucuzza R, Greco R. Corrosion effects on the capacity and ductility of concrete half-joint bridges. Construct Build Mater. 2022;360:129555. https://doi.org/10.1016/j.conbuildmat.2022.129555
10. Martinelli P, Colombo M, di Prisco M. Robustness assessment of half-joint RC girder bridges. Eng Struct. 2024;306:117712. https://doi.org/10.1016/j.engstruct.2024.117712
11. Di Carlo F, Meda A, Molaioni F, Rinaldi Z. Experimental evaluation of the corrosion influence on the structural response of Gerber half-joints. Eng Struct. 2023;285:116052. https://doi.org/10.1016/j.engstruct.2023.116052
12. Mata-Falcón J, Pallarés L, Miguel PF. Proposal and experimental validation of simplified strut-and-tie models on dapped-end beams. Eng Struct. 2019;183:594–609. https://doi.org/10.1016/j.engstruct.2019.01.010
13. Belletti B, Calcavecchia B, Ferretti D, Ravasini S. Capacity assessment of uncorroded and corroded dapped-end beams by NLFE and strut-and-tie based methods. Struct Concr. 2024;25:1275–304. https://doi.org/10.1002/suco.202301020
14. Spinella N, Messina D. Load-bearing capacity of Gerber saddles in existing bridge girders by different levels of numerical analysis. Struct Concr. 2023;24:211–26. https://doi.org/10.1002/suco.202200279

15. Santarsiero G, Masi A, Picciano V. Durability of gerber saddles in RC bridges: analyses and applications (Musmeci bridge, Italy). Inf Dent. 2021;6:6. https://doi.org/10.3390/infrastructures6020025
16. Desnerck P, Lees JM, Morley CT. Impact of the reinforcement layout on the load capacity of reinforced concrete half-joints. Eng Struct. 2016;127:227–39. https://doi.org/10.1016/j.engstruct.2016.08.061
17. Granata MF, Messina D, Colajanni P, La Mendola L, Lo GE. Performance of a historical cantilever reinforced concrete bridge with half-joint degradation. Structure. 2022;37:561–75. https://doi.org/10.1016/j.istruc.2022.01.039
18. Mitchell D, Marchand J, Croteau P, Cook WD. Concorde overpass collapse: structural aspects. J Perform Constr Facil. 2011;25:25–553. https://doi.org/10.1061/(asce)cf.1943-5509.0000183
19. di Prisco M, Colombo M, Martinelli P. Structural aspects of the collapse of a RC half-joint bridge: case of the Annone overpass. J Bridg Eng. 2023;28:28. https://doi.org/10.1061/jbenf2.beeng-6063
20. Desnerck P, Lees JM, Morley CT. The effect of local reinforcing bar reductions and anchorage zone cracking on the load capacity of RC half-joints. Eng Struct. 2017;152:865–77. https://doi.org/10.1016/j.engstruct.2017.09.021
21. Desnerck P, Lees JM, Morley CT. Strut-and-tie models for deteriorated reinforced concrete half-joints. Eng Struct. 2018;161:41–54. https://doi.org/10.1016/j.engstruct.2018.01.013
22. Mak MWT, Lees JM. Bond strength and confinement in reinforced concrete. Construct Build Mater. 2022;355:129012. https://doi.org/10.1016/j.conbuildmat.2022.129012
23. Kotsovou G, Vougioukas E, Cotsovos DM. Application of strut-and-tie models for assessing RC half-joints not complying with current code specifications. Acta Polytech. 2022;62:607–17. https://doi.org/10.14311/AP.2022.62.0607
24. Brencich A, Bovolenta R, Ghiggi V, Pera D, Redaelli P. Rebound hammer test: an investigation into its reliability in applications on concrete structures. Adv Mater Sci Eng. 2020;2020:1–11. https://doi.org/10.1155/2020/6450183
25. Cristofaro MT, Viti S, Tanganelli M. New predictive models to evaluate concrete compressive strength using the SonReb method. J Build Eng. 2020;27:100962. https://doi.org/10.1016/J.JOBE.2019.100962
26. International Atomic Energy Agency (IAEA). Guidebook on non-destructive testing of concrete structures. Training course series No. 17. Vienna: IAEA; 2002.
27. Dewar J, Collis L, Llewellin J, Murphy W, Plowman JM, Warren PA, et al. Concrete core testing for strength. Technical report n.11 of a concrete society working party. London: Concrete Society; 1987.
28. Tukey JW. Exploratory data analysis. Reading, MA: Addison-Wesley; 1977.
29. EC Innovation Programme IN30902I. CONTECVET a validated users manual for assessing the residual service life of concrete structures. 2001.
30. ASTM Standard G1-90. Standard practice for preparing, cleaning, and evaluating corrosion test specimens. West Conshohocken: ASTM; 1999.
31. Torres-Acosta AA, Martínez-Madrid M. Residual life of corroding reinforced concrete structures in marine environment. J Mater Civ Eng. 2003;15:344–53. https://doi.org/10.1061/(asce)0899-1561(2003)15:4(344)
32. Vidal T, Castel A, François R. Analyzing crack width to predict corrosion in reinforced concrete. Cem Concr Res. 2004;34:165–74. https://doi.org/10.1016/S0008-8846(03)00246-1
33. González JA, Andrade C, Alonso C, Feliu S. Comparison of rates of general corrosion and maximum pitting penetration on concrete embedded steel reinforcement. Cem Concr Res. 1995;25:257–64. https://doi.org/10.1016/0008-8846(95)00006-2
34. Val DV, Melchers RE. Reliability of deteriorating RC slab bridges. J Struct Eng. 1997;123:1638–44. https://doi.org/10.1061/(asce)0733-9445(1997)123:12(1638)
35. Andrade C, Oller S, Trujillo FJP. Basis for calculation the residual mechanical properties of corroding bars. Struct Concr. 2023;24:257–68. https://doi.org/10.1002/suco.202200310
36. Kagermanov A, Markovic I. An overview on finite element-modelling techniques for structural capacity assessment of corroded reinforced concrete structures. Struct Infrastruct Eng. 2022;19:1–15. https://doi.org/10.1080/15732479.2022.2045612
37. Cairns J, Plizzari GA, Du Y, Law DW, Franzoni C. Mechanical properties of corrosion-damaged reinforcement. ACI Mater J. 2005;102:256–64. https://doi.org/10.14359/14619
38. Du YG, Clarkt LA, Chan AHC. Effect of corrosion on ductility of reinforcing bars. Mag Concr Res. 2005;57:407–19. https://doi.org/10.1680/macr.2005.57.7.407
39. Morinaga S. Remaining service life of reinforced concrete structure after corrosion cracking. In: Sjöström C, editor. Durability of building materials & components, 7. Volume 1. London: E & FN Spon; 1996. p. 127–37.
40. Imperatore S, Rinaldi Z, Drago C. Degradation relationships for the mechanical properties of corroded steel rebars. Construct Build Mater. 2017;148:219–30. https://doi.org/10.1016/j.conbuildmat.2017.04.209
41. Miluccio G, Losanno D, Parisi F, Cosenza E. Traffic-load fragility models for prestressed concrete girder decks of existing Italian highway bridges. Eng Struct. 2021;249:113367. https://doi.org/10.1016/j.engstruct.2021.113367
42. Wong PS, Vecchio FJ, Trommels H. Vector2 and formworks user's manual. 2nd ed. Toronto: University of Toronto; 2013.
43. Vecchio FJ, Collins MP. The modified compression field theory for RC elements subjected to shear. J Am Concr Inst. 1986;83:219–31. https://doi.org/10.14359/10416
44. Vecchio FJ. Disturbed stress field model for reinforced concrete: formulation. J Struct Eng. 2000;126:1070–7. https://doi.org/10.1061/(asce)0733-9445(2000)126:9(1070)
45. Mander JB, Priestley MJN, Park R. Theoretical stress-strain model for confined concrete. J Struct Eng. 1988;114:1804–26. https://doi.org/10.1061/(asce)0733-9445(1988)114:8(1804)
46. Bentz EC. Sectional analysis of reinforced concrete members. Ph.D. thesis. University of Toronto, Toronto. 2000.
47. Ramberg W, Osgood WR. Description of stress-strain curves by three parameters. Washington: National Advisory Committee Aeronautics; 1943.
48. Červenka V, Jendele L, Červenka J. ATENA program documentation part 1 theory. Prague: Červenka Consulting; 2020.
49. Červenka J, Papanikolaou VK. Three dimensional combined fracture-plastic material model for concrete. Int J Plast. 2008;24:2192–220. https://doi.org/10.1016/j.ijplas.2008.01.004

50. Menetrey P, Willam KJ. Triaxial failure criterion for concrete and its generalization. ACI Struct J. 1995;92:311–8. https://doi.org/10.14359/1132
51. Fédération Internationale du Béton. fib model code for concrete structures 2010. Lausanne: Fédération Internationale du Béton; 2013.
52. European Committee for Standardization. Eurocode 2: Design of Concrete Structures – part. 1–1: general rules and rules for buildings (EN 1992-1-1:2004). Brussels: European Committee for Standardization; 2005.
53. Tuutti K. Corrosion of steel in concrete. Doctoral thesis (monograph). Division of Building Materials, Lund University, Stockholm. 1982.
54. Monteiro AV, Gonçalves A. Probabilistic assessment of the depassivation limit state of reinforced concrete structures based on inspection results. J Build Eng. 2022;49:104063. https://doi.org/10.1016/j.jobe.2022.104063
55. Hájková K, Šmilauer V, Jendele L, Červenka J. Prediction of reinforcement corrosion due to chloride ingress and its effects on serviceability. Eng Struct. 2018;174:768–77. https://doi.org/10.1016/j.engstruct.2018.08.006
56. Bertolini L, Elsener B, Pedeferri P, Polder R. Corrosion of steel in concrete: prevention, diagnosis, repair. Weinheim: WILEY-VCH Verlag GmbH & Co. KGaA; 2005. https://doi.org/10.1002/3527603379
57. Fick AV. On liquid diffusion. London Edinburgh Dublin Philos Mag J Sci. 1855;10:30–9. https://doi.org/10.1080/14786445508641925
58. Andrade C, Alonso C. Recommendations of RILEM TC-154-EMC: "electrochemical techniques for measuring metallic corrosion" test methods for on-site corrosion rate measurement of steel reinforcement in concrete by means of the polarization resistance method. Mater Struct. 2004;37:623–43. https://doi.org/10.1007/BF02483292
59. Andrade C, Linger L. Verification of durability of new and existing structures through the design, construction and operational phases. Struct Concr. 2023;24:4377–86. https://doi.org/10.1002/suco.202201177
60. Kwon SJ, Na UJ, Park SS, Jung SH. Service life prediction of concrete wharves with early-aged crack: probabilistic approach for chloride diffusion. Struct Saf. 2009;31:75–83. https://doi.org/10.1016/j.strusafe.2008.03.004
61. Kwon S-J, Na U-J. Prediction of durability for RC columns with crack and joint under carbonation based on probabilistic approach. Int J Concr Struct Mater. 2011;5:11–8. https://doi.org/10.4334/ijcsm.2011.5.1.011
62. Yang LF, Ma Q, Yu B. Analytical solution and experimental validation for dual time-dependent chloride diffusion in concrete. Construct Build Mater. 2018;161:676–86. https://doi.org/10.1016/j.conbuildmat.2017.11.176
63. Gino D, Castaldo P, Bertagnoli G, Giordano L, Mancini G. Partial factor methods for existing structures according to *fib* bulletin 80: assessment of an existing prestressed concrete bridge. Struct Concr. 2020;21:15–31. https://doi.org/10.1002/SUCO.201900231
64. Bentz EC, Vecchio FJ, Collins MP. Simplified modified compression field theory for calculating shear strength of reinforced concrete elements. ACI Struct J. 2006;103:614. https://doi.org/10.14359/16438
65. Fédération Internationale du Béton (fib). *Fib* model code for concrete structures 2020 (final draft). Lausanne: Fédération Internationale du Béton. 2023.
66. Nielsen MP, Hoang LC. Limit analysis and concrete plasticity. 3rd ed. Boca Raton: CRC Press; 2016.
67. De Domenico D, Ricciardi G. Shear strength of RC beams with stirrups using an improved Eurocode 2 truss model with two variable-inclination compression struts. Eng Struct. 2019;198:109359. https://doi.org/10.1016/j.engstruct.2019.109359
68. De Domenico D. Torsional strength of RC members using a plasticity-based variable-angle space truss model accounting for non-uniform longitudinal reinforcement. Eng Struct. 2021;228:111540. https://doi.org/10.1016/j.engstruct.2020.111540
69. Wight JK, MacGregor JG. Reinforced concrete: mechanics and design. 6th ed. Upper Saddle River: Pearson Education Limited; 2012.
70. Schlaich J, Schaefer K, Jennewein M. Toward a consistent design of structural concrete. PCI J. 1987;32:74–150. https://doi.org/10.15554/pcij.05011987.74.150
71. Schlaich J, Schäfer K. Design and detailing of structural concrete using strut-and-tie models. Struct Eng. 1991;69:113–25.
72. Arya C. Design of Structural Elements: concrete, steelwork, masonry and timber designs to British standards and Eurocodes. 3rd ed. Oxon: Spon Press; 2009. https://doi.org/10.1201/b18121
73. Sigrist V, Bentz E, Ruiz MF, Foster S, Muttoni A. Background to the *fib* model code 2010 shear provisions – part I: beams and slabs. Struct Concr. 2013;14:195–203. https://doi.org/10.1002/suco.201200066
74. De Domenico D, Messina D, Recupero A. A combined experimental–numerical framework for assessing the load-bearing capacity of existing PC bridge decks accounting for corrosion of prestressing strands. Materials. 2021;14:4914. https://doi.org/10.3390/ma14174914
75. FIB International. *fib* Task Group 2.5. *fib* Bulletin 106 – advances on bond in concrete, state of art report. Lausanne: Fédération Internationale du Béton (*fib*). 2022. https://doi.org/10.35789/fib.BULL.0106. Accessed on 15 December 2024.

AUTHOR BIOGRAPHIES

Dario De Domenico, Department of Engineering, University of Messina, Messina, Italy. Email: dario.dedomenico@unime.it.

Nino Spinella, Department of Civil Engineering and Architecture, University of Catania, Catania, Italy. Email: nino.spinella@unict.it.

Davide Messina, Department of Engineering, University of Messina, Messina, Italy. Email: davide.messina@unime.it.

Matteo Mazzeo, Department of Engineering, University of Messina, Messina, Italy. Email: matteo.mazzeo@unime.it.

Antonino Recupero, Department of Engineering, University of Messina, Messina, Italy. Email: antonino.recupero@unime.it.

How to cite this article: De Domenico D, Spinella N, Messina D, Mazzeo M, Recupero A. Structural behavior of deteriorated Gerber half-joints in highway overpasses by nonlinear finite element analysis combined with a simplified uniform-corrosion model. Structural Concrete. 2025;26(5):5677–707. https://doi.org/10.1002/suco.202400556